



Report on the calibrated reservoir
model for the super-hot reservoir at
Los Humeros and its calibration
against available field data

D 6.6

Report on the calibrated reservoir model for the super-hot reservoir at Los Humeros and its calibration against available field data

D 6.6

Version 1.0

Part 1 - Paromita Deb, Dominique Knapp, Gabriele Marquart (RWTH Aachen)

Part 2- Giordano Montegrossi (CNR Florence) Work package 6

08 May 2019

Website: <http://www.gemex-h2020.eu>



The GEMex project is supported by the European Union's Horizon 2020 programme for Research and Innovation under grant agreement No 727550

Table of Contents

List of figures	5
List of tables	7
Executive Summary	8
1 PART 1 – RWTH Aachen	9
1.1 Introduction	9
1.2 Local reservoir model	9
1.2.1 Modelled lithological units	9
1.2.2 Grid discretization and parameterization of numerical model	10
1.3 Basic mathematical model equations	12
1.4 Data for calibration	13
1.5 Boundary Conditions	16
1.6 Permeability of the main structural elements for reservoir scale model	20
1.7 Results	21
1.7.1 Influence of sealing condition of Los Humeros rim fault	21
1.7.2 Impact of increasing permeability of the fault structures within the Los Potreros caldera	22
1.7.3 Additional model: impact of increasing intrinsic permeability of andesite	24
1.7.4 Mean temperature maps for all model realisations	25
1.8 Conclusion and discussion	29
1.9 References	31
2 PART 2 – CNR	35
2.1 Introduction	35
2.2 Objective	35
2.3 Data Available	35
2.3.1 Reservoir engineering: feed zones, temperature and pivot point	35
2.3.2 Temperature log interpretation	36
2.3.3 Pressure log interpretation	37
2.3.4 Results of temperature and pressure log interpretation	38
2.4 Recharge path and water table	41
2.5 Hot source	43
2.6 Feed zones and geological model	45
2.7 Permeability and porosity	48
2.8 Thermal capacity and conductivity	51
2.9 Numerical model	52
2.9.1 Grid discretization	54
2.9.2 Boundary conditions	55
2.9.3 Steady state	56
2.9.4 Calibration	59
	3

2.10	<i>References</i>	61
	Appendix A - Wellbore fluid flow modeling	62

List of figures

- Figure 1.1: Revised regional geological map of the Los Humeros Caldera Complex (Carrasco-Núñez et al., 2017); the regional scale model covers the entire map area while the blue outline indicates the boundary of the local reservoir model, the modelled faults within the reservoir boundary are overlaid on the map for visualisation 9
- Figure 1.2: Reservoir model (top right) extracted from the regional model (top left), modelled units in reservoir scale are indicated in different colours (bottom)..... 11
- Figure 1.3: Los Humeros geology and fault system: left figure showing the main caldera structures in regional scale and the reservoir model boundary indicated in blue; the right figure shows some of the wells within the reservoir model referred in this report; black shapes represent the faults; black dots are dry and uneconomic wells and red dots represent the good producers..... 17
- Figure 1.4: Top: staggered temperature field (left) and corresponding standard deviations (right) for 6 regional model scenarios at 1000 m.a.s.l. Bottom: staggered field of hydraulic head referenced to the model bottom (left) and corresponding standard deviations for all six model scenarios at 1000 m.a.s.l. (right), coordinates are w.r.t. model point coordinates and have the same extent as in the geological map in Figure 1. 18
- Figure 1.5: Staggered temperature fields and standard deviation of temperature for the three fault permeability scenarios, comparing the impact of permeability anisotropy within the limestone and the andesite sections; coordinates are w.r.t. model point coordinates and have the same extent as in the geological map in Figure 1.1.. 19
- Figure 1.6: Staggered hydraulic head field and standard deviation of hydraulic head for the three fault permeability scenarios, comparing the impact of anisotropy within the limestone and the andesite sections. 20
- Figure 1.7: Effect of regional boundary conditions on the reservoir scale temperature model extracted at 1000 m.a.s.l., left: boundary condition with closed Los Humeros and Los Potreros rim faults, fault permeability of 10^{-17} m^2 is assigned to the caldera rims (Scenario 1a), right: boundary condition with open Los Humeros and Los Potreros rim faults (Scenario 3a), fault permeability of 10^{-15} m^2 is assigned to caldera rim faults 22
- Figure 1.8: Effect of increasing fault permeability on the temperature distribution, top: simulated with boundary conditions from Scenario 1a (closed LH and LP caldera rims) and presented in order of increasing fault permeability from left to right, bottom: simulated with boundary conditions from Scenario 3a (open LH and LP caldera rim) and presented in order of increasing fault permeability from left to right; fault permeability values used is indicated in the bottom of the figure in black 23
- Figure 1.9: Effect of increased andesite permeability on the temperature distribution, model plane at 1000 m.a.s.l.; permeability of andesite is indicated at the top of the figures, respectively..... 24
- Figure 1.10: Mean temperature distribution (left) and standard deviation (right) extracted at 500 masl (top) and 1000 m.a.s.l. (bottom) within the reservoir model boundary obtained by staggering temperature fields from total 18 realisations (three different fault permeability scenarios simulated using six different boundary conditions) 25
- Figure 1.11: Mean temperature distribution (left) and standard deviation (right) extracted at 1500 m.a.s.l (top), 2000 m.a.s.l (middle) and 2500 m.a.s.l. (bottom) within the reservoir model boundary obtained by staggering temperature fields from total 18 realisations (three different fault permeability scenarios simulated using six different boundary conditions)..... 26
- Figure 1.12: Mean temperature map extracted at 1000 m.a.s.l. showing well positions in different colors to indicate the overall match of the simulated temperature with bottomhole corrected temperature of wells, the black dots are well locations where the simulated temperature shows a good match with the bottom hole corrected temperature data, the well locations indicated in white and yellow show a mismatch of $30^\circ\text{C} - 50^\circ\text{C}$ 27

Figure 1.13: Good match between BHT for different well positions (black point - Horner corrected, blue point - spherical corrected BHT) and temperature extracted along respective well positions for different realisations indicated by colored lines.	28
Figure 1.14: Mismatch between BHT for some well positions (black point - Horner corrected, blue point - spherical corrected BHT) and temperature extracted along respective well positions for different realisations indicated by colored lines	29
Figure 1.15: Overestimated BHT temperatures for wells H-24 and H-25 (black point - Horner corrected, blue point - spherical corrected BHT) and temperature extracted along respective well positions for different realisations indicated by colored lines	29
Figure 2.1: Well H-49, central area. Here is an example of heating up profiles with the shallow and deep feed zones evidenced. In the figure, the Flowing Well temperature log (Dynamic log) is shown, and a non-flowing zone at the level of deep feed zone could be observed. In this case, the temperature of the dynamic log (flowing section) could be clearly related to the temperature of the shallow feed zone	37
Figure 2.2: Well H-49, central area. Pressure profiles during heating up show a steam zone (nearly 0-1300 m depth), and a liquid zone, in which a Pivot point could be observed at 1450 m depth with 82 bar.	38
Figure 2.3: Pressure of Pivot point vs Depth	40
Figure 2.4: Temperature distribution vs Depth	41
Figure 2.5: PT Diagram	41
Figure 2.6: Stable Isotope distribution and boiling model	42
Figure 2.7: Hydraulic head (elevation of the water table in masl) in the area surrounding Los Humeros (the study area is evidenced as green rectangle, arbitrary elevation).	42
Figure 2.8: Bicarbonate in liquid phase, as representative of the recharge component evidenced in the geochemical investigation (Task 4.3)	43
Figure 2.9: Temperature distribution at the deep feed zone.....	44
Figure 2.10: Boron distribution, from geochemical modeling Task 4.3	45
Figure 2.11: Resulting resistivity sections across the caldera edifice, Arzate et al., 2018, on left, and resistivity profile obtained during GEMEX project on right.....	45
Figure 2.12: Feed zones position with the neighbouring geological layers from the local geological model of Los Humeros.....	46
Figure 2.13: Detail of the deep Feed zone with Top Basement and Top Pre-Caldera unit, top - view from south west, bottom -view from west.	47
Figure 2.14: Detail of the shallow Feed zone with Top Basal Pre-Caldera unit and Inter Pre-Caldera unit -view from south west.	48
Figure 2.15: Hawkin's radial model schematic	49
Figure 2.16: Theis model of pumping step test from well H-43	50

Figure 2.17: Porosity and permeability investigation on andesite from Los Humeros geothermal field	50
Figure 2.18: Permeability of Colima volcano with respect to confining pressure	51
Figure 2.19: Los Humeros Andesite heat capacity vs temperature	52
Figure 2.20: Los Humeros andesite thermal conductivity vs temperature	52
Figure 2.21: Geological map of Los Humeros with the modeled area	54
Figure 2.22: Recharge boundary	55
Figure 2.23: Temperature distribution at 0 masl (left figure) and with the 2-phase zone (figure on right, violet cloud is the 2-phase zone)	56
Figure 2.24: Temperature distribution at 500 m asl. The 3 temperature anomaly could be identified.	57
Figure 2.25: Temperature distribution, view from east, with the 400°C bottom boundary condition (dark orange surface).....	58
Figure 2.26: Temperature distribution, with a slice at -250 m asl, and the 400°C bottom boundary condition (dark orange surface).....	59
Figure 2.27: Model calibration: modeled temperature vs temperature from well logs (measured temperature)	60
Figure 2.28: Temperature and pressure profile from wellbore model compared with temperature and pressure from dynamic log.....	63
Figure 2.29: Dryness profile, where dryness is steam flow divided by total flow	63

List of tables

Table 1.1: Groups and units modelled in WP 3; for WP 6 modelling we divided Group IV into two units to separate the sedimentary limestone from the crystalline basement	10
Table 1.2: Parameterization of the rock units of the reservoir model	11
Table 1.3: Bottom hole temperatures for Los Humeros wells corrected using two different methods (Horner, spherical radial flow method (SRF)); some wells reach stabilised temperatures at certain depths and do not require correction, these are reported under Stabilised temperature; Reduced level implies depth above mean sea level ..	15
Table 1.4: Permeability values and anisotropy factors for different fault sealing conditions used in this study (anisotropy factor in z-direction is 1)	17
Table 2.1: Results from well logs investigation, feed zones position and temperature with pivot point position and pressure	39

Executive Summary

Work Package 6 of the GEMex project aims to characterise the superhot geothermal reservoir of Los Humeros and the engineered geothermal system (EGS) reservoir of Acoculco in terms of fluid and rock properties, heat transfer and flow conditions.

Los Humeros is situated in the Trans Mexican Volcanic Belt and is of high interest because of its unconventional geothermal characteristics. In spite of being under commercial exploitation for almost four decades, the superhot reservoirs of Los Humeros still demands research to fully understand the heat source, the geochemistry of the fluid and the interplay between different fluid pathways. The conceptual geological ideas of both the fields are poorly understood and are subjects of study within GEMex.

This report describes the approaches used for simulating the natural steady state behaviour of fluid flow and heat transport of Los Humeros geothermal field. It is divided into parts. Part 1 documents the contribution of RWTH Aachen University towards initial state modeling of Los Humeros in reservoir scale, which is a continuation of report D 6.3. Part 2 of this report is a contribution of CNR and describes an alternate approach used for initial state modeling of Los Humeros.

The major differences between the two approaches are the different structural models used and the simulation codes. At RWTH Aachen, we used the structural models created within WP 3 for numerical modeling. The code used for simulation is Shemat-Suite which uses finite difference method to solve the partial different equations numerically; while at CNR, modeling is performed using Tough 2 which uses finite element model and the structural model used is defined by the feeding zones obtained from temperature logs from wells.

1 PART 1 – RWTH Aachen

(Paromita Deb, Dominique Knapp)

1.1 Introduction

Part 1 of this report is a continuation of Deliverable D 6.3 which provides the introduction to the Los Humeros geothermal field, geology of the area and describes in details the regional scale simulations performed in order to obtain reasonable boundary conditions for modeling the heat transfer and fluid flow processes on a smaller reservoir scale. In the following sections, we briefly recall the work performed in the regional scale model and then describe the simulations of the reservoir scale models.

Figure 1.1 shows the geological map which is used as a reference to create the structural model of Los Humeros. The model extends 56 km in the EW direction and 36 km in the NS direction. The smaller reservoir model indicated by the blue boundary in Figure 1.1 extends 9.5 km in EW and 12.5 km in NS direction. The vertical extent for both the models is 12 km (down to 7 km below mean sea level). Los Humeros is located at an elevation of approximately 2800 m.a.s.l. For reservoir modeling purpose, we restricted our model to 3 km below sea level to reduce impact of uncertain rock types on our model. The total vertical extent of our reservoir model is around 6.5 km. [Deliverable D 6.3](#) describes the geological units and the petrophysical data used for populating the model units.

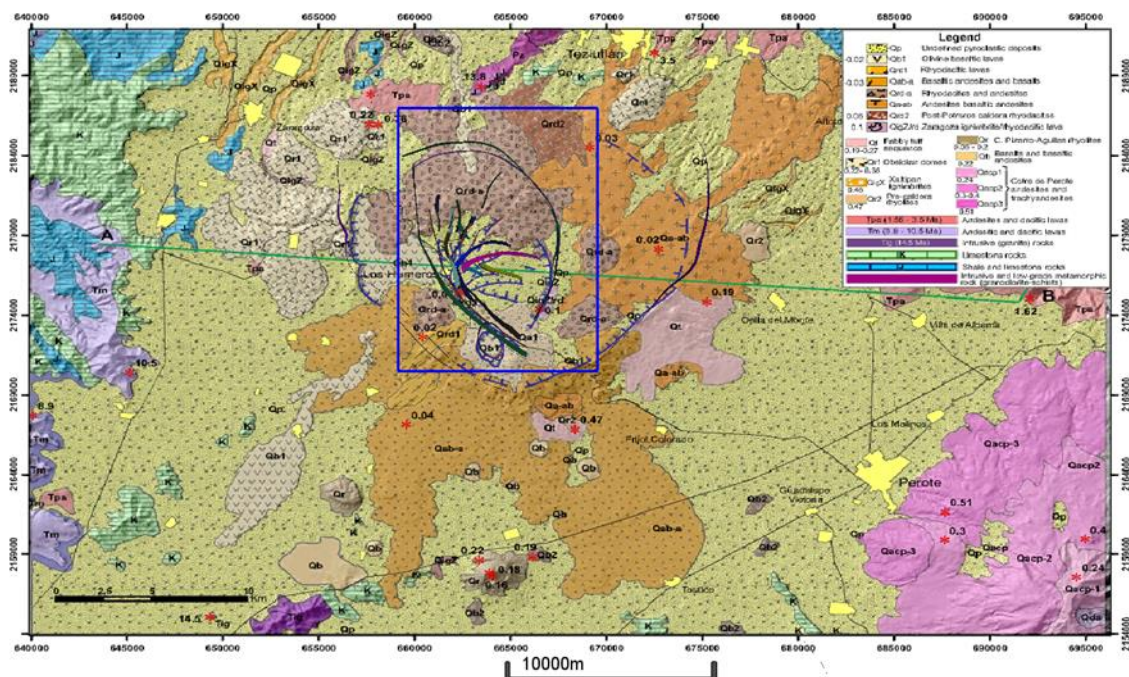


Figure 1.1: Revised regional geological map of the Los Humeros Caldera Complex (Carrasco-Núñez et al., 2017); the regional scale model covers the entire map area while the blue outline indicates the boundary of the local reservoir model, the modelled faults within the reservoir boundary are overlaid on the map for visualisation

1.2 Local reservoir model

1.2.1 Modelled lithological units

The reservoir model constructed in WP 3 comprises of 9 units as shown in Table 1.1. Details on the workflow and data used is available in Calcagno (2018). In addition to the 9 units modelled by WP 3, we

divided Unit 9 (Basement) into two separate units – sedimentary limestone and the crystalline basement part. This was done to account for the different thermal and hydraulic properties of the rock types which are modelled together as Group IV in the structural model provided by WP 3. The thickness of the limestone basement was estimated to be not larger than 3000 m in the area of Los Humeros (Norini, 2015). From the lithology record of well H-24 we know that in the bottom-hole depth at 340 m below sea level limestone is still encountered. Due to lack of any other information on the exact border between crystalline and sedimentary basement, we separated both groups at a depth of 600 m below mean sea level (i. e. at a depth of about 3.4 km below the surface).

Table 1.1: Groups and units modelled in WP 3; for WP 6 modelling we divided Group IV into two units to separate the sedimentary limestone from the crystalline basement

Groups	Units	Rock description	Age (Ma)
Group I: Post-caldera volcanism	U1 Undefined pyroclastic	Tuffs, pumices, & some alluvium	< 0.003
	U2 Post caldera	Rhyodacites, andesites, basaltic andesites, and olivine basalts lava flows, with ages between	0.05 and 0.003
Group II: Caldera volcanism	U3 Los Potreros caldera	Rhyodacitic flows and Zaragoza Ignimbrites	0.069
	U4 Intermediate caldera	Faby Tuff & andesitic-dacitic lava flows (0.27 to 0.19 Ma)	0.07
		Rhyolitic and obsidian domes (0.36 to 0.22 Ma)	0.074
	U5 Los Humeros caldera	Mainly the Xaltipan Ignimbrite with minor andesitic and rhyolitic lavas (Quaternary)	0.165
Group III: Pre-caldera volcanism	U6 Upper pre-caldera	Rhyolites, dacites, some andesites and tuffs and minor basalts	0.693 to 0.155
	U7 Intermediate pre-caldera	Mainly pyroxene andesites (Teziultán Andesites) with mafic andesites in the basal part and/or dacites (Plio-Quaternary)	2.61 to 1.46
	U8 Basal pre-caldera	Mainly hornblende andesites (Alseseca Andesites & Cerro Grande) and dacites - Miocene	10.5 to 8.9
Group IV: Limestone Basement	U9 Basement	Middle Miocene granitic intrusions	15.12
		Cretaceous limestones and shales and minor flint	~140
		Jurassic limestones and shales	~190
Group IV: Crystalline Basement	U10 Basement	Paleozoic granites and schists (Teziultán Massif)	> 251

1.2.2 Grid discretization and parameterization of numerical model

The reservoir scale model covers an area of 118.75 km² and is defined by the blue boundary in Figure 1.1. Within the simulation program Shemat-Suite, it is discretised in small cells of dimension 50 m × 50 m × 50 m and consists of a total of 617500 numerical grids. Figure 1.2 shows the modelled units used for Shemat-Suite.

Table 1.2 summarises the petrophysical properties for each unit obtained from laboratory measurements performed in task 6.1 and literature data wherever there were not enough sample measurements.

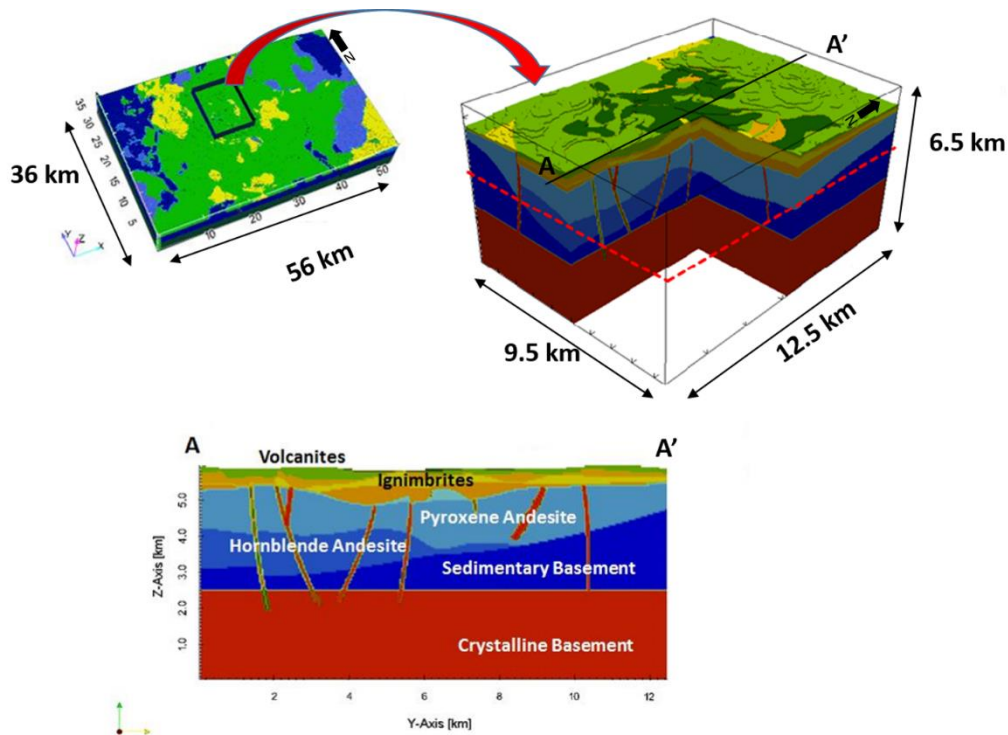


Figure 1.2: Reservoir model (top right) extracted from the regional model (top left), modelled units in reservoir scale are indicated in different colours (bottom)

Table 1.2: Parameterization of the rock units of the reservoir model

Lithology	Porosity [%]			Matrix Thermal Conductivity [W/(m K)]			Permeability (intrinsic) [m ²]			Heat Production Rate [uW/m ³]*	Volumetric heat capacity [J/(m ³ K)]		
	Mean	Std. dev.	N	Mean	Std. dev.	N	Mean	Std. dev.	N	Mean	Mean	Std. dev.	N
Unit 1: Pumice, ash fall deposits, some alluvium	50.01	1.00	5	1.91	0.10	5	1.27E-14	2.52E-15	5	0.5	2016751	22722	1
Unit 2: Basalts, Rhyodacites, Andesites, Olivine Basalts	12.80	2.60	19	2.18	0.23	11	1.18E-15	2.78E-15	16	0.5	2035034	79063	2
Unit 3: Zaragoza Ignimbrites	14.30	1.96	15	2.74	0.13	14	1.17E-17	6.96E-18	10	1.48	2117271	154843	5
Unit 4: Rhyolitic and obsidian domes, fabby tuffs and andesitic - dacitic lava flows	12.13	0.60	4	2.31	0.12	3	8.00E-16	1.40E-15	6	1.5	1992487	151008	7
Unit 5: Xaltipan Ignimbrites	14.30	1.96	15	2.74	0.13	14	1.17E-17	6.96E-18	10	1.48	2117271	154843	5
Unit 6: Rhyolites, dacites and few andesites and tuffs	12.13	0.60	4	2.31	0.12	3	8.00E-16	1.40E-15	6	1.8	1992487	151008	7
Unit 7: Pyroxene Andesites (30% porous/70% massive) ***	6.00	1.73	-	2.14	0.17	7	1.36E-16	1.12E-16	10	1.08	2140839	158948	16
Unit 8: Hornblende Andesites (30% porous/70% massive) ***	6.00	1.73	-	2.63	0.33	9	2.14E-16	1.79E-16	10	1.08	2127233	123154	13
Unit 9a: Limestones	2.02	1.96	28	2.77	0.17	20	3.00E-18	6.00E-18	24	0.62	2201903	195816	1
Unit 9a: Cherts/Marble/Skarn	1.44	1.53	32	4.20	0.56	20	6.80E-18	1.42E-17	20	0.62	2337680	427144	3
Unit 9a: Limestones 95% (Cherts/Marble/Skarn ~ 5%)	1.99	1.94	50	2.84	0.19	40	3.19E-18	6.41E-18	44	0.62	2208692	207382	4
Unit 9b: Granites/Granodiorites /Schists/Phyllites	2	1	-	3.2**	0.32**	-	3.00E-18	6.00E-18	-	2.45	2730075**	534374**	-

(*compiled from literature values from Rybach (1976, 1986); **values for c_p and λ compiled from Schön (2004);*** bimodal distribution of porosity assumed, values calculated using a 70 % massive, 30 % porous rock mass). Unit 9b (predominantly granites) was assigned an intrinsic permeability on the order of 3×10^{-18} m² (no laboratory measurements available)

1.3 Basic mathematical model equations

For numerical simulation the finite differences code SHEMAT-Suite (Rath et al., 2006) is used. SHEMAT-Suite is based on SHEMAT (Simulator for Heat and Mass Transport; Clauser, 2003) and solves the coupled steady state or transient equations for groundwater flow, heat and reactive solute transport. For our modelling of the natural state of Los Humeros geothermal field, we restrict ourselves to a steady state modelling of the initial temperature and pressure fields, due the unclear conceptual model ideas of the heat source and the lack of information corresponding to the cooling history, the position and the size of possible magma chambers or pockets, which are needed for performing a detailed modelling of the time dependent heat transport in the field before production started. This workflow implies to assume the system to be in equilibrium state before production.

The steady state mass conservation of water in a porous medium is expressed by the continuity equation, where h represents the hydraulic head, Q labels the source and sink term, \mathbf{k} is the permeability tensor, ρ_f and μ_f are density and dynamic viscosity of the pore fluid, respectively and g represents the gravity acceleration

$$\nabla \left(\frac{\rho_f g}{\mu_f} \mathbf{k} \nabla h \right) + Q = 0 \quad (1)$$

The physical properties of water in sub-critical and super-critical conditions are calculated using the correlations provided by the International Association for the Properties of Water and Steam (Wagner et al., 2000). The pore water pressure (P) is calculated according to the head distribution and the depth z , given by the definition of de Marsily (1986), where P_0 represents the pressure at the surface for $z=0$:

$$P(z, h) = P_0 + \int_0^z \rho_f(\bar{z}) g (h - \bar{z}) d\bar{z} \quad (2)$$

Heat transport due to conduction, advection and radiogenic heat production is expressed in the energy conservation equation in steady state

$$(\rho c)_f \mathbf{v} \nabla T - \nabla (\lambda_e \nabla T) = A \quad (3)$$

The equation consists of an advective term, yielding Darcy velocity \mathbf{v} , fluid density ρ_f and fluid specific heat capacity c_f , a diffusive term, comprising the effective thermal conductivity of the rock-fluid mixture λ_e and a heat production term A .

Groundwater flow and Darcy velocity \mathbf{v} are described by Darcy's Law:

$$\mathbf{v} = \frac{k}{\mu_f}(\nabla p - \rho_f g) \quad (4)$$

Observations of production data from numerous wells of Los Humeros show that the field was liquid dominated prior to its commercial exploitation. It is estimated that in the beginning of 1990, the liquid saturation was about 90% which decreased to 50% in 2012 (Arellano, 2018) due to lack of sufficient recharge and hence considerable pressure depletion. Therefore, we consider an initial liquid dominated reservoir and account for the supercritical conditions of water in the deep part of the reservoir by calculating the physical properties of water using the correlations by the International Association for the Properties of Water and Steam (Wagner et al., 2000).

Rock thermal conductivity depends on the rock type but generally decreases with temperature (Zoth and Hänel, 1988). It is important to know the representative values of thermal conductivity with temperature and pressure for thermal modelling. In the Los Humeros model, however there exists several rock types which are grouped together into one unit and hence it is difficult to isolate the influence of each rock type, i. e. to determine the effective thermal conductivity. The dominant part of the regional model domain is made up by limestone basement intercalated with shales and metamorphosed to skarn and marble in the contact aureoles. This is overlain by igneous and metamorphic rocks (pre-caldera and caldera deposits). On the reservoir scale model, the relative contribution of metamorphic and igneous rocks are more than the limestone deposits. The relationship proposed by Sekiguchi (1984) provided the best theoretical fit for the temperature dependency of thermal conductivity of igneous and metamorphic rocks when compared to experimentally measured data in the temperature range from 0°C to 500°C (Lee and Deming, 1998). Therefore, we used the correction proposed by Sekiguchi (1984) to account for the dominant igneous and magmatic rock compounds within the model domain.

The formula implements the temperature correction for matrix thermal conductivity λ_m on basis of a given matrix conductivity at room temperature $\lambda_{m,0}$ and the actual temperature T and was included in the manner of Pasquale et al. (2017):

$$\lambda_m(T) = 1.8418 + (\lambda_{m,0} - 1.8418) \left(\frac{1}{0.002732 T + 0.7463} - 0.2485 \right) \quad (5)$$

Effective thermal conductivity of the fluid filled porous rock λ_e is dependent on porosity, ϕ , fluid thermal conductivity λ_f and rock matrix thermal conductivity λ_m . It is calculated according to the geometric mean (Clauser, 2003):

$$\lambda_e = \lambda_f^\phi \lambda_m^{(1-\phi)} \quad (6)$$

1.4 Data for calibration

Comisión Federal de Electricidad (CFE) provided temperature logs run after drilling from almost 52 wells. These were used as primary information for the purpose of modeling to constrain temperature-depth distribution. The temperature data is affected due to mud circulation and strong interflow between the

feeding zones. Therefore the data needed to be corrected in order to obtain information about the formation temperature at bottom depth of the wells. We used two different methods to correct the data – Horner method described by equation 7 and a second method based on the assumption of spherical radial heat flow at the bottom of the well described by equation 8. Further details regarding the equations can be found in [Deliverable D 6.3](#).

Horner's method is described by the following equation:

$$T_{ws} = T_i - C \log \left(\frac{t + t_c}{t} \right), \quad (7)$$

where T_{ws} is the shut-in temperature at time t , T_i is the stabilised formation temperature at infinite shut-in time and t_c is the mud circulation time. This model describes a straight line with slope C and intercept T_i . T_i is obtained by extrapolation to infinite shut-in time.

The Spherical Radial Heat Flow (SRF) method is based on the following equation

$$T_{ws} = T_i - C \frac{1}{\sqrt{t}} \quad (8)$$

A plot of shut-in temperature T_{ws} versus the inverse of the square root of shut-in time describes a straight line with slope C and intercept, T_i (the static formation temperature at infinite shut in time).

For Los Humeros wells, it is observed that the temperatures calculated using equation 8 are higher than the values obtained from Horner's method (equation 7). Garcia-Gutierrez (2002) suggested that equation 8 provides static temperatures that are closer to the true formation temperatures in the Los Humeros geothermal field. Temperatures corrected using both methods for bottom-hole depth for the Los Humeros wells are presented in Table 1.3. As these corrected temperatures serve as a critical information towards verification of the numerical model of Los Humeros, we use temperatures obtained from both equations as bounding limits for calibrating our numerical model at bottom-hole depth of wells. The lower bound is defined by corrected temperature from Horner's method while temperatures obtained from equation 8 (SRF) is used as the upper bound.

It should be noted that not all Los Humeros wells are used for calibrating our model. The commercial exploitation of the field began in the year 1990. Wells drilled after that period have not been used for calibration.

Table 1.3: Bottom hole temperatures for Los Humeros wells corrected using two different methods (Horner, spherical radial flow method (SRF)); some wells reach stabilised temperatures at certain depths and do not require correction, these are reported under Stabilised temperature; Reduced level implies depth above mean sea level

Wells	X	Y	Elevation	Depth of correction	Reduced level	Stabilised	Horner	SRF
			(m.a.s.l.)	(m)	(m.a.s.l.)	(°C)	(°C)	(°C)
H-1-D	661906	2175064	2828	1815	1013		237.38	268.61
H-2-V	662646	2172435	2896	2298	598		277.72	297.4
H-3-V	660622	2177903	2755	1659	1096		274.38	326.87
H-5-V	660540	2175950	2754	1845	909		231.65	251.69
H-6-V	663508	2173545	2894	2540	354		316.35	348.92
H-7-V	661838	2175871	2782	2281	501		300.84	337.22
H-8-V	661582	2176392	2771	2300	471		394.03	456.99
H-11-D	662574	2177436	2812	1460	1352		281.33	310.29
H-13-D	662244	2177406	2835	1850	985		268.26	288.84
H 13-V	662244	2177406	2835	2401	434		303.43	329.64
H-14-V	663832	2169627	2815	1373	1442		116.5	144.08
H-16-V	661557	2178250	2783	2038	745		318.16	369.36
H-18-V	664916	2172077	3002	2885	117		294	332.02
H-21-V	662279	2179691	2871	2214	657		276.16	300.7
H-22-V	660055	2178853	2763	1539	1224		268.81	297.95
H-24-V	665497	2172938	2922	3263	-341		259	288.05
H-25-V	666393	2176169	2800	2283	517		194.63	223.32
H-28-V	662601	2177741	2819	2558	261	361		
H-29-D	661884	2177843	2807	2186	621	352		
H-31-V	661832	2179041	2810	1914	896		315.67	349.97
H-32-V	662631	2178043	2818	2186	632		332.13	362.97
H-38-V	661897	2178155	2795	1390	1405		166.23	189.76
H-39-V	663365	2173291	2890	2495	395		255.31	286.89

1.5 Boundary Conditions

In order to assign proper temperature and pressure boundary conditions for the local reservoir model, preparatory simulations are performed in the regional scale model. Figure 1.3 (left) shows the extent of the preliminary regional model (extent of the map), the reservoir model boundary (indicated in blue) and the main Los Humeros caldera structure. In Figure 1.3 (right), the black shapes indicate the modelled faults within the reservoir model boundary and some well locations referred in this report are presented in dots.

The model currently available is based mainly on well data and surface geological observations. Absence of field scale geophysical data imposes a strong structural uncertainty in the model. The depth of the small local faults are assumed to be equal to the observed extent of their surface manifestations. The larger main faults are considered to extent maximum to the brittle-ductile transition zone. In addition, the sealing conditions of faults are unknown. The Los Humeros and Los Potreros caldera faults might significantly affect the recharge to the geothermal system depending on their sealing condition. Sealing conditions of the main caldera rim faults are not widely discussed in the available literature. The fault rims could be partially mineralised and limiting fluid flow or may be completely closed and act as impermeable barriers to fluid flow. To account for these under-determined configurations of the caldera annular fault structures, several scenarios were simulated in the regional scale. The main configurations tested in the regional model are

- Scenario 1: Los Humeros Caldera rim and Los Potreros Caldera rim closed to flow (indicated by very low permeability 10^{-17} m^2 in both the caldera rim structures),
- Scenario 2: Los Humeros Caldera rim closed and Los Potreros Caldera rim open to flow (indicated by 10^{-17} m^2 for Los Humeros and 10^{-15} m^2 for Los Potreros),
- Scenario 3: Los Humeros Caldera rim and Los Potreros Caldera rim open to flow (indicated by 10^{-15} m^2 for both Los Humeros and Los Potreros).

Each scenario is further simulated with isotropic and anisotropic permeability configurations for the host rocks, i.e. the andesites and the limestones. As the preferential flow paths in fractured reservoirs are expected to be vertical, we reduced the horizontal permeability components (k_x and k_y) for andesites. In case of limestones within platform deposits we expect a horizontally layered structure and corresponding horizontal preferential flow direction (k_x and k_y are doubled). The scenarios are shown in Table 1.4.

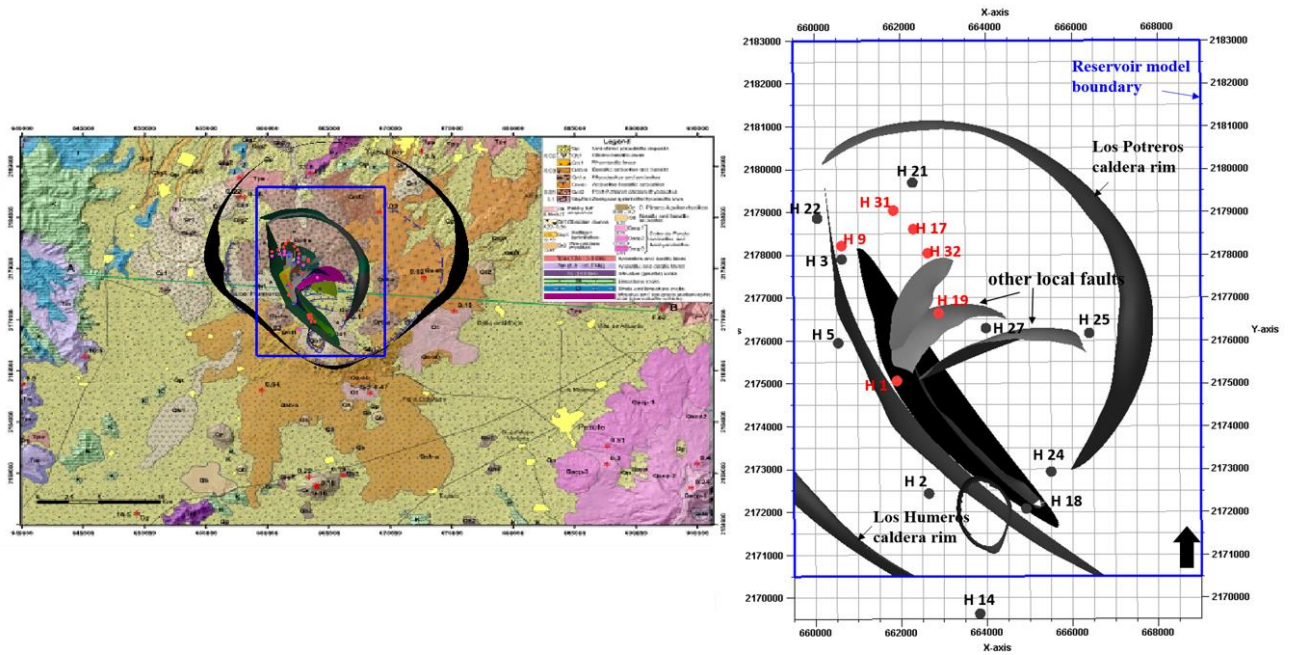


Figure 1.3: Los Humeros geology and fault system: left figure showing the main caldera structures in regional scale and the reservoir model boundary indicated in blue; the right figure shows some of the wells within the reservoir model referred in this report; black shapes represent the faults; black dots are dry and uneconomic wells and red dots represent the good producers.

Table 1.4: Permeability values and anisotropy factors for different fault sealing conditions used in this study (anisotropy factor in z-direction is 1)

Scenario	LH rim perm [m ²]	LP rim perm [m ²]	Fault perm inner caldera [m ²]	Limestone anisotropy factor x-, y- direction		Andesite anisotropy factor x-, y- direction	
Scenario 1a	2.0×10^{-17}	2.0×10^{-17}	3.0×10^{-15}	1	1	1	1
Scenario 1b	2.0×10^{-17}	2.0×10^{-17}	3.0×10^{-15}	2	2	0.5	0.5
Scenario 2a	2.0×10^{-17}	2.0×10^{-15}	3.0×10^{-15}	1	1	1	1
Scenario 2b	2.0×10^{-17}	2.0×10^{-15}	3.0×10^{-15}	2	2	0.5	0.5
Scenario 3a	2.0×10^{-15}	2.0×10^{-15}	3.0×10^{-15}	1	1	1	1
Scenario 3b	2.0×10^{-15}	2.0×10^{-15}	3.0×10^{-15}	2	2	0.5	0.5

All model scenarios were simulated individually. Since the fault sealing conditions and the extent of fracturing are not well known, we regard the various scenarios as equally likely. Therefore, we staged the results to investigate the spatial distribution of uncertainty in reservoir temperature and pressure.

In Figure 1.4, we present the mean temperature map and standard deviation resulting from the above six scenarios extracted at a depth of 1000 m.a.s.l. (corresponds to almost 1800 m depth from topography). This map represents the cumulative effect in temperature field as a result of different sealing conditions of the Los

Humeros caldera fault and the Los Potreros fault as well as effect of anisotropy in intrinsic permeability of limestones and andesites.

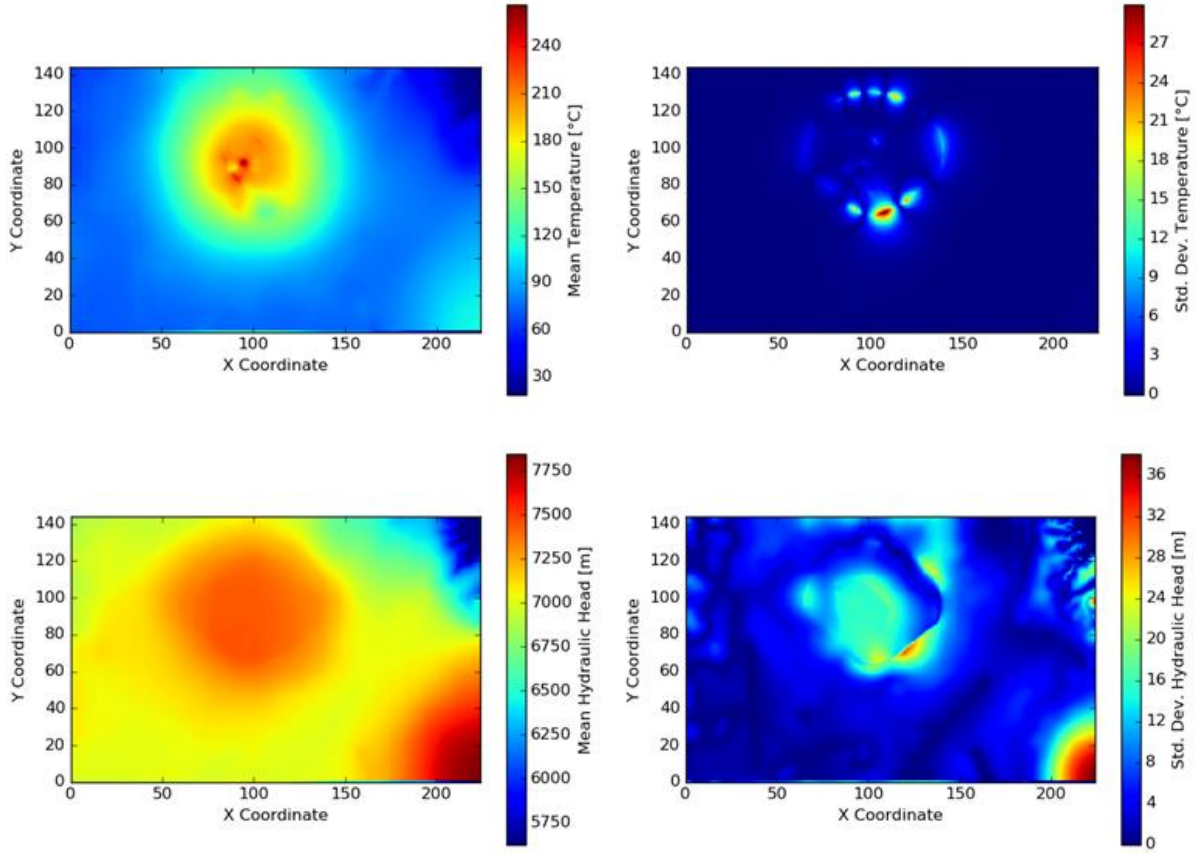


Figure 1.4: Top: staggered temperature field (left) and corresponding standard deviations (right) for 6 regional model scenarios at 1000 m.a.s.l. Bottom: staggered field of hydraulic head referenced to the model bottom (left) and corresponding standard deviations for all six model scenarios at 1000 m.a.s.l. (right), coordinates are w.r.t. model point coordinates and have the same extent as in the geological map in Figure 1.

From Figure 1.4 (top), it is clear that the main difference in temperature is caused as a result of opening or closing of Los Humeros caldera rim fault, with an uncertainty in temperature of about 20 °C. The maximum standard deviation of the temperature is ~30 °C in the south-east corner of the Los Humeros caldera rim.

Similar effects can be observed on the head differences in the regional scenarios (Figure 1.4, bottom). The average head changes between all six scenarios with a maximum standard deviation ~38 m within the limestone outcrop at the lower right corner of the regional model domain. Within the caldera and at the caldera rims, standard deviation of hydraulic head varies in the order of 8 m to 32 m resulting from the closing and opening of the main fault features.

The effect of permeability anisotropy in temperature field can be observed in Figure 1.5. The mean temperature and standard deviation presented in these figures are obtained from the temperature field for isotropic and anisotropic permeability conditions corresponding to each fault sealing scenario. For example in Figure 1.5 (top), mean and standard deviation are calculated from temperature field simulated using Scenario 1a and Scenario 1b of Table 1.4. If we compare only the standard deviation in temperature resulting from anisotropy, we observe that anisotropy influences the temperature within the inner caldera, with maximum standard deviations of around 5 °C when Los Humeros caldera is closed (Figure 1.5 (top) - Scenario 1a and 1b and Figure 1.5 (middle) - Scenario 2a and 2b). The impact of anisotropy almost doubles

(10 °C standard deviation) when Los Humeros Caldera fault is open to flow (Figure 1.5 (bottom) - Scenario 3a and 3b).

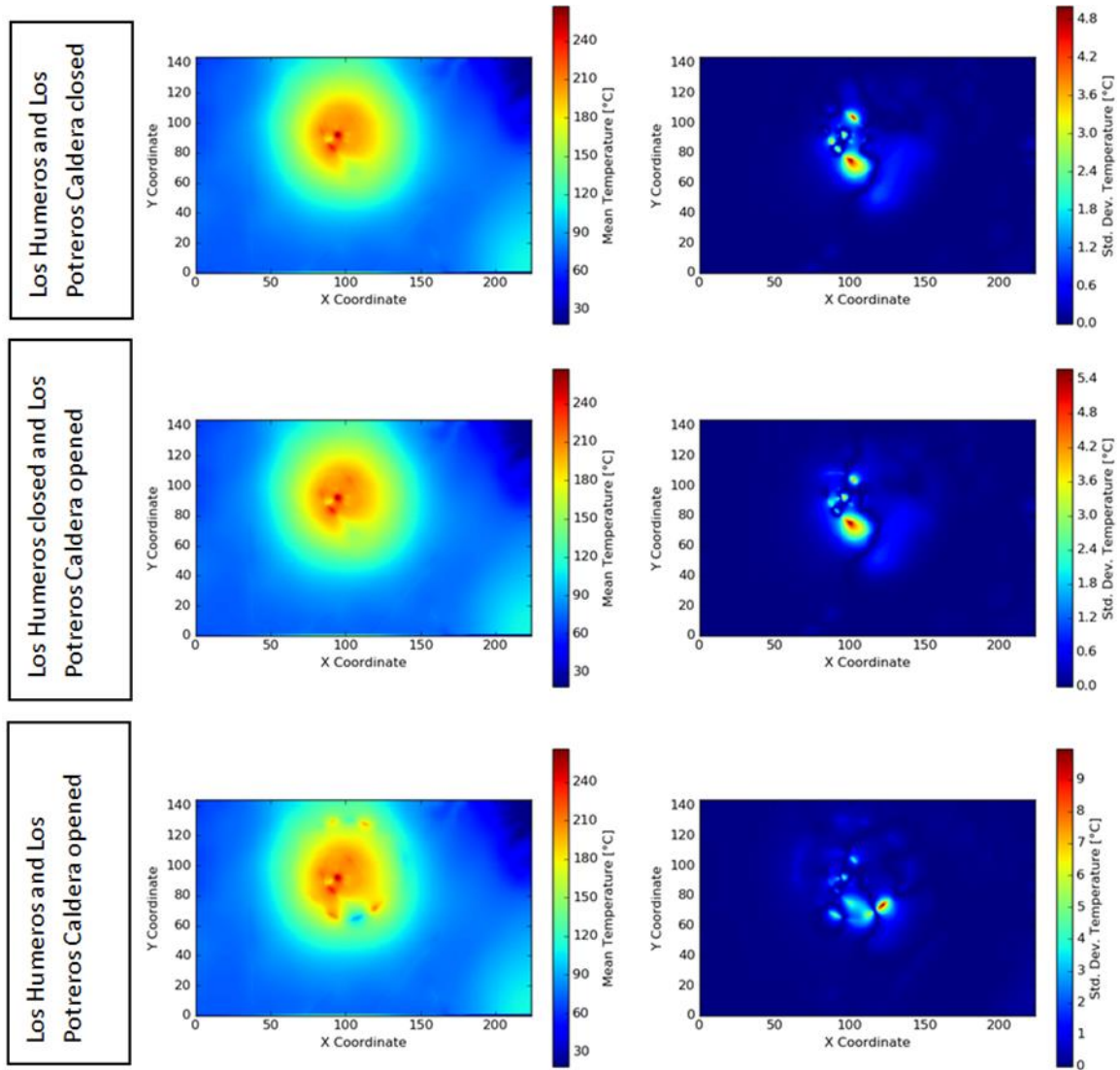


Figure 1.5: Staggered temperature fields and standard deviation of temperature for the three fault permeability scenarios, comparing the impact of permeability anisotropy within the limestone and the andesite sections; coordinates are w.r.t. model point coordinates and have the same extent as in the geological map in Figure 1.1.

In Figure 1.6, we compare the effect of anisotropy in hydraulic head for different fault sealing scenarios. A closer look on the influence of anisotropy on each fault permeability scenario lines out, that anisotropy mainly affects again the inner caldera region. The effect of anisotropy is most pronounced when assuming the Los Humeros Caldera rim fault as open for flow (Figure 1.6, bottom) especially at the south-east border of Los Humeros caldera rim.

This observation can be related to the geometry of the andesite outcrop which is only covered by a successively thinning ignimbrite seal from the central caldera to the south-east. In Figure 1.2 (bottom), a N-S cross section, A-A' indicates the thinning ignimbrite towards the south. The opening of Los Humeros fault and an applied permeability anisotropy (with higher permeability in vertical direction) within the andesite unit therefore leads to small scale convection cells in the Los Humeros rim fault affecting predominately the south-eastern area. Comparing the different fault scenarios, this effect is as well inhibited by closing Los

Humeros fault. The additional closure of Los Potreros caldera rim fault does not result in notable temperature variations but only in strong head differences along its rim.

The differences in temperature and head in the regional model caused due to different scenarios result in different boundary conditions for the reservoir model. As all the scenarios are equally probable, we extracted the boundary conditions corresponding to all six regional scenarios and used them for the reservoir scale modeling.

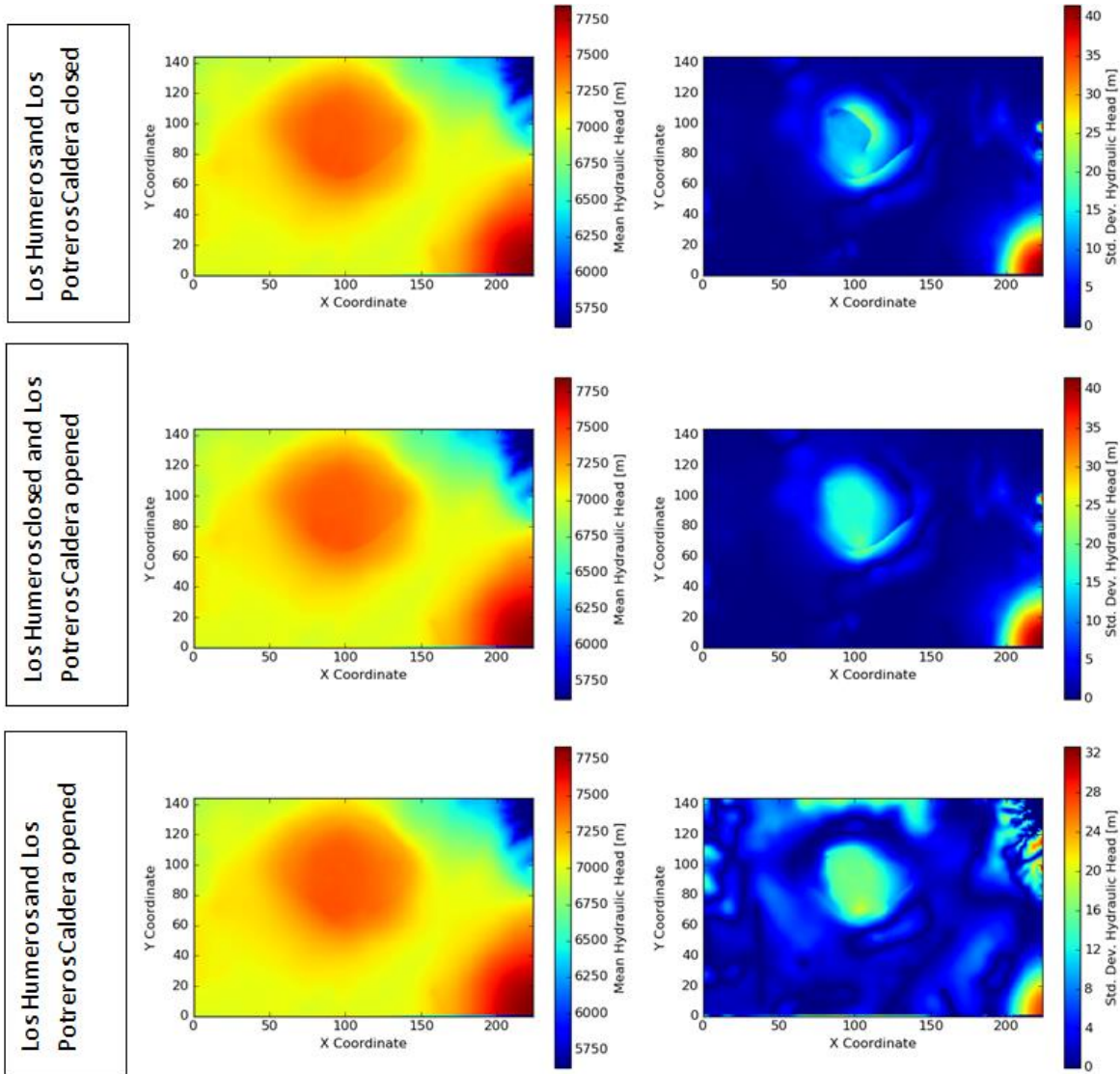


Figure 1.6: Staggered hydraulic head field and standard deviation of hydraulic head for the three fault permeability scenarios, comparing the impact of anisotropy within the limestone and the andesite sections.

1.6 Permeability of the main structural elements for reservoir scale model

The flow in the wells of Los Humeros is driven by the interconnected fractures and faults. This is evident considering that the geothermal system is composed of very low porous and low permeability volcanic rocks as the host rocks. So far, the production reported from CFE is considered to be from the andesite sections. Evaluation of temperature logs allows us to identify feeding zones located within the andesites.

The measured intrinsic permeability of the andesites within Los Humeros area is on the order of $1.8 \times 10^{-16} \text{ m}^2$ (refer Table 1.2). This value is comparable to results of studies performed on intact andesites in the low porosity range of 3 % - 4 %, which show permeability values on the order of $2 \times 10^{-16} \text{ m}^2$ to $2 \times 10^{-17} \text{ m}^2$ (Heap and Kennedy, 2016). In comparison to conventional reservoirs, we therefore expect the andesite sections only to have good reservoir qualities in locally highly fractured areas, related to faulting, connecting vesicular porosity and creating fracture networks which are effective to flow.

In this study, we assume that the production zones/feeding zones observed in the wells are structurally controlled and occur wherever the andesite or the limestone zones are intersected by the main faults giving rise to damaged zones composed of interconnected fractures within the andesites and limestones. We restrict the high permeability zones along the mapped and implemented fault structures of the local reservoir model. In our model, the faults are mapped as zones extending between 50 m and 100 m laterally and vertically limited by the modelled depth. In reality damaged zones from faults can extend for several hundred meters giving rise to a widely spread productive well behavior.

To obtain a reliable permeability estimate, we used information obtained from pressure transient analysis of the production wells. Transmissivities calculated from some of the transient pressure tests (wells H-1, H-6, H-9, H-17, H-18, etc.) indicate a permeability thickness on the order of 10^{-13} m^3 to 10^{-15} m^3 (unpublished, data analysis by A. Aragon, INEEL). Additional studies from Sánchez Luviano et al. (2015) indicated an average permeability thickness of the reservoir in the order of $3.98 \times 10^{-13} \text{ m}^3$. Aragón et al. (2008) reported permeability within a range of $1.97 \times 10^{-15} \text{ m}^2$ to $1.68 \times 10^{-14} \text{ m}^2$ from analysis of inflow type curves of thirteen production wells of Los Humeros, which is in agreement with a 10 m to 100 m wide productive zone. These permeability values obtained from different wells provides a general estimate of the permeability controlled by the structures. In the numerical simulation, we assigned a range of permeability to the local faults and evaluated their impact on the temperature field and the hydraulic head of the reservoir. Permeability for the fault structures are assigned according to the range obtained from the transient pressure tests from $5 \times 10^{-16} \text{ m}^2$ to $5 \times 10^{-15} \text{ m}^2$ increased by half an order of magnitude at each step. Due to numerical instability, fault permeability values higher than $5 \times 10^{-15} \text{ m}^2$ (5 mD) could not be tested. We also present results of some additional simulations where we evaluated the impact of increased intrinsic permeability in andesite.

1.7 Results

1.7.1 Influence of sealing condition of Los Humeros rim fault

In Figure 1.7, we present temperature maps extracted from reservoir model simulation at 1000 m.a.s.l. simulated using two extreme boundary conditions – Scenario 1a and Scenario 3a. The depth used in these figures is 1000 m.a.s.l. due to the fact that andesites which are the host rocks and contains the feeding zones in the wells are encountered at this depth. Figure 1.7 (left) shows the simulated temperature using boundary condition extracted from the regional convective simulation Scenario 1a where both Los Humeros and Los Potreros caldera rims are closed (permeability assigned to the caldera rims is 10^{-17} m^2). This scenario implies that the caldera rim faults are sealed due to mineralization and have negligible contribution to fluid flow. If compared to the right temperature map on Figure 1.7 which is extracted at the same depth level but simulated using boundary condition from regional convective Scenario 3a (permeability two orders of magnitude higher than Scenario 1a), we observe a strong impact on the temperature field in the south-east corner of the figure. In Scenario 3a, both the caldera rim faults are open to flow. The shape of the isotherms does not change significantly between the two scenarios, however a decrease in temperature of at least 40 °C is observed in the south-east quadrant of Los Potreros caldera. This is caused as a result of strong influx of cold

water through the rim faults of Los Humeros which is not sealed in Scenario 3a (open fault boundary condition) and contributes to fluid flow.

These results indicate the significance of the knowledge of the sealing condition of the caldera rim faults. It is important to note that opening or closing of caldera rim faults causes a considerable change in the influx of cold water wherever the sealing layer, ignimbrite is absent. In zones where thick ignimbrite layers are present, the sealing condition causes less perturbation in the temperature field. This can be observed in the central part of the field where opening or closing of Los Potreros does not significantly alter the temperatures.

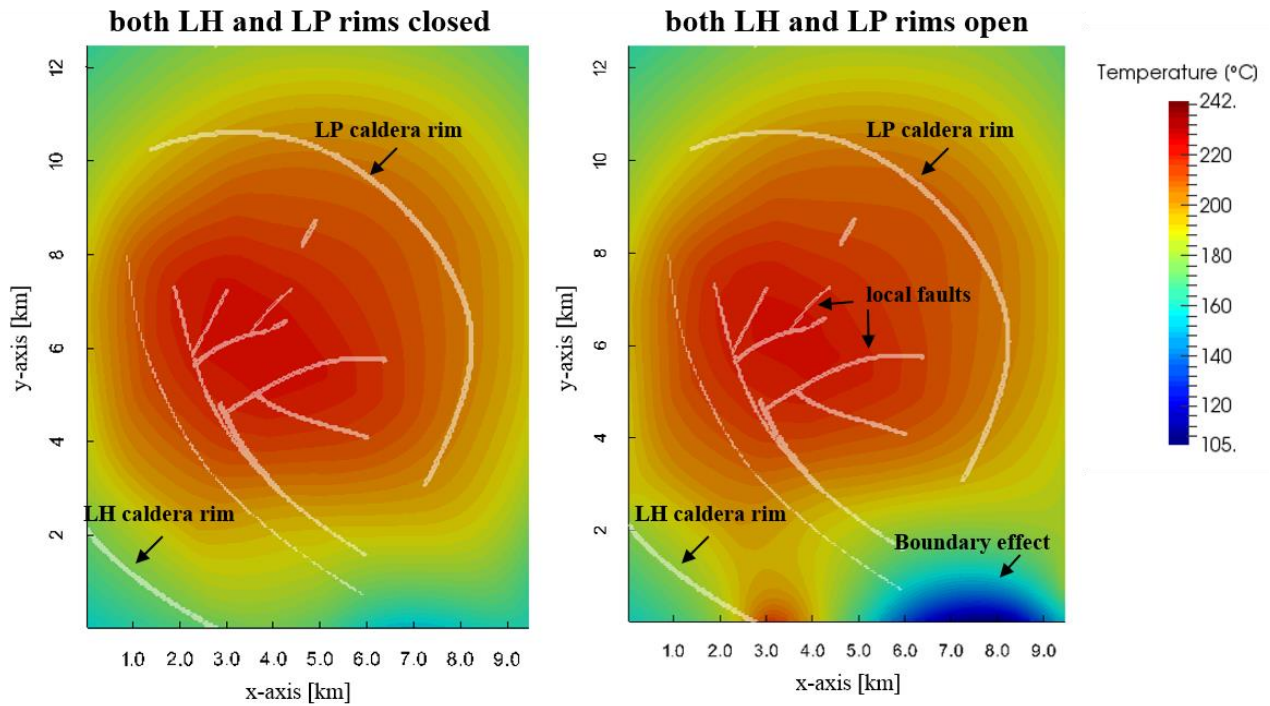


Figure 1.7: Effect of regional boundary conditions on the reservoir scale temperature model extracted at 1000 m.a.s.l., left: boundary condition with closed Los Humeros and Los Potreros rim faults, fault permeability of 10^{-17} m^2 is assigned to the caldera rims (Scenario 1a), right: boundary condition with open Los Humeros and Los Potreros rim faults (Scenario 3a), fault permeability of 10^{-15} m^2 is assigned to caldera rim faults

1.7.2 Impact of increasing permeability of the fault structures within the Los Potreros caldera

In Figure 1.8, we examine the impact of increasing the permeability of the local faults (within the LP caldera rim) on the temperature distribution within the Los Humeros reservoir model. These fault structures are shown in Figure 1.3 (right) as well as Figure 1.7 (right) as local faults. We assume these faults to act as the main structural elements responsible for fluid flow and heat transfer in the currently producing LH geothermal field. The top three figures represent temperature map extracted at 1000 m.a.s.l. using boundary conditions of Scenario 1a (closed caldera rims) in order of increasing permeability of the local faults: $5 \times 10^{-16} \text{ m}^2$, 10^{-15} m^2 and $5 \times 10^{-15} \text{ m}^2$, while the bottom three figure represents similar map extracted using boundary conditions from Scenario 3a.

The effect of increasing permeability of the local faults can be noted when comparing the figures with fault permeability $5 \times 10^{-16} \text{ m}^2$ and $5 \times 10^{-15} \text{ m}^2$. For both scenarios, 1a (top figures) and 3a (bottom figures), an increase in temperature of around 20 - 25 °C with increasing permeability is observed at the centre of the caldera where several fault intersect. This increase in temperature is irrespective of the boundary condition used and can be related to the upwelling zones and intersection of permeable faults with these zones. Interestingly wells which encountered very high temperature gradient ($> 15 \text{ }^\circ\text{C}/100 \text{ m}$), for example H 31, H 32, H 22, etc., are located in this part of the field.

It is interesting to note that the increasing fault permeability does not impact the temperature distribution of the entire area uniformly. Towards the southern end of the NW-SE trending local faults indicated by the dashed grey outline in Figure 1.8 top right and bottom right, a cold zone is created which decreases the temperature by atleast 15 °C as the fault permeability values increase. Investigation of thickness of different lithology in this area leads us to conclude that this effect is related to the total absence or negligible thickness of ignimbrites which act as sealing layers. Therefore significant influx of cold water perturbs the temperature field in areas where ignimbrites are absent and faults form effective pathways. However, the effect of fault permeability on temperature in the range studied is not more than about 15 °C at its maximum, increasing with depth.

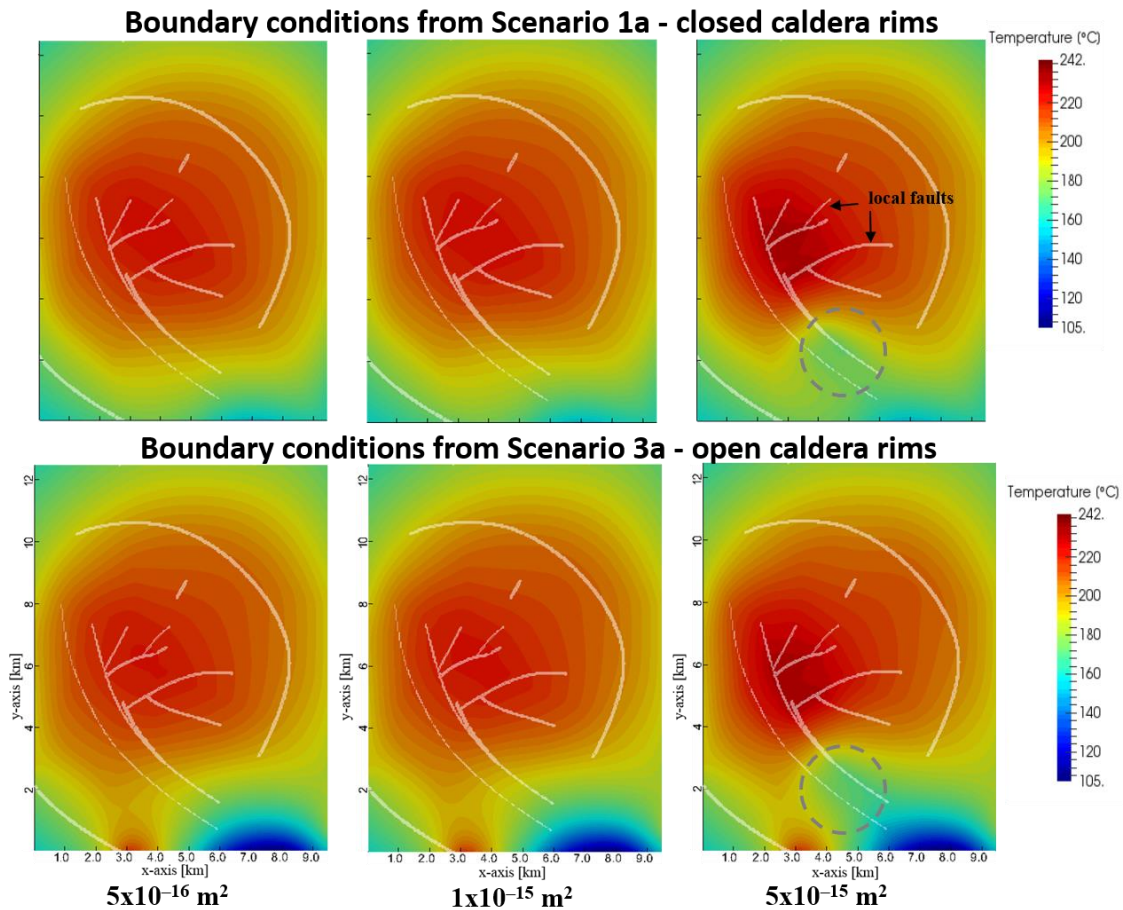


Figure 1.8: Effect of increasing fault permeability on the temperature distribution, top: simulated with boundary conditions from Scenario 1a (closed LH and LP caldera rims) and presented in order of increasing fault permeability from left to right, bottom: simulated with boundary conditions from Scenario 3a (open LH and LP caldera rim) and presented in order of increasing fault permeability from left to right; fault permeability values used is indicated in the bottom of the figure in black

It can be noted that a change in fault permeability by only half an order of magnitude impacts the temperature by 10 °C – 12 °C difference. The fault permeability considered in the simulations are relatively low and can be much higher in magnitude depending on the extent of the fault affected zone or much lower in case of extended precipitation of minerals in the pathways. The figures are however an indicative of the fault permeability related impact on the temperature distribution.

However, the most significant difference in temperature between the top three (Figure 1.8 top) and the bottom three (Figure 1.8 bottom) models is the presence of the cold zone in the south-eastern corner of the model. This cold zone reduces the temperature in this part of the field by at least 40 – 50 °C. This is caused due to the boundary condition of Scenario 3a whereby Los Humeros fault is open to fluid flow and is explained in Section 1.6.1.

Similar effect is observed if andesite permeability is increased leading to stronger influx of cold water in these zones. This is explained in the following section.

1.7.3 Additional model: impact of increasing intrinsic permeability of andesite

The intrinsic permeability of the andesite rocks as evaluated from the laboratory measurements lies between $1 - 2 \times 10^{-16} \text{ m}^2$. This variation of the model is performed by increasing the intrinsic permeability of andesite by a factor of two ($2 \times 10^{-16} \text{ m}^2$). In all the other scenarios, $1 \times 10^{-16} \text{ m}^2$ is assigned to the andesites. This scenario is run with an objective of investigating the effect of uncertain intrinsic permeability on the temperature field at the reservoir depth. A permeability value of $5 \times 10^{-15} \text{ m}^2$ is assigned to all the local faults. Figure 1.9 compares the temperature distribution at 1000 m.a.s.l. with andesite permeability $1 \times 10^{-16} \text{ m}^2$ (Figure 1.9, left) and doubled andesite permeability (Figure 1.9, right).

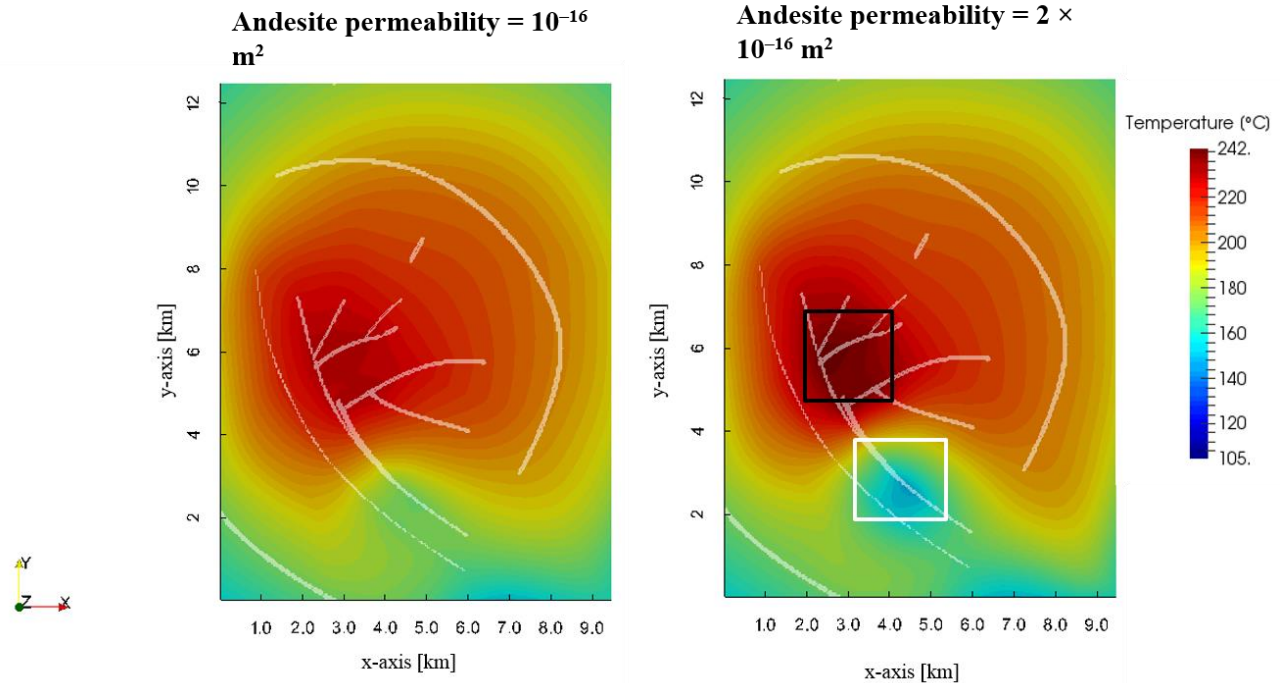


Figure 1.9: Effect of increased andesite permeability on the temperature distribution, model plane at 1000 m.a.s.l.; permeability of andesite is indicated at the top of the figures, respectively.

It is interesting to note that towards the central west of the Los Potreros caldera (indicated by the black box in Figure 1.9, right), the temperature increases by 15 °C – 20 °C, while in the south-east of the Los Potreros

caldera (indicated by the white box in Figure 1.9, right), there is an opposite effect and the temperature drops down by 20 °C – 25 °C. This contrasting effect is probably also created as a result of the thickness of sealing layer on top of the andesite. Increasing andesite permeability results in increased influx of cold water from the surface in areas where the sealing layers are absent. However a contrasting effect is seen where the sealing layers act as good barriers limiting the influx of cold water. Stronger upwelling zones are created at reservoir depth (i.e. 1000 m.a.s.l which is about 1.8 km below the surface) due to increased permeability resulting in corresponding temperature increase.

1.7.4 Mean temperature maps for all model realisations

In this section, we present the mean and standard deviation of the temperature field at particular depths created by staggering simulated temperature distributions using different boundary conditions and geological scenarios.

In the following figures, we present depth slices of staggered temperature maps simulated using the six boundary conditions obtained from the regional convective scenarios. The six boundary conditions include the effect of open and closed Los Humeros and Los Potreros caldera rim faults and additionally consider the anisotropy in fluid flow in the andesites and limestones. The temperature maps at various depths provide an overall mean temperature which can be expected in this area under different structural configurations of the rim faults and with varying fault permeability values.

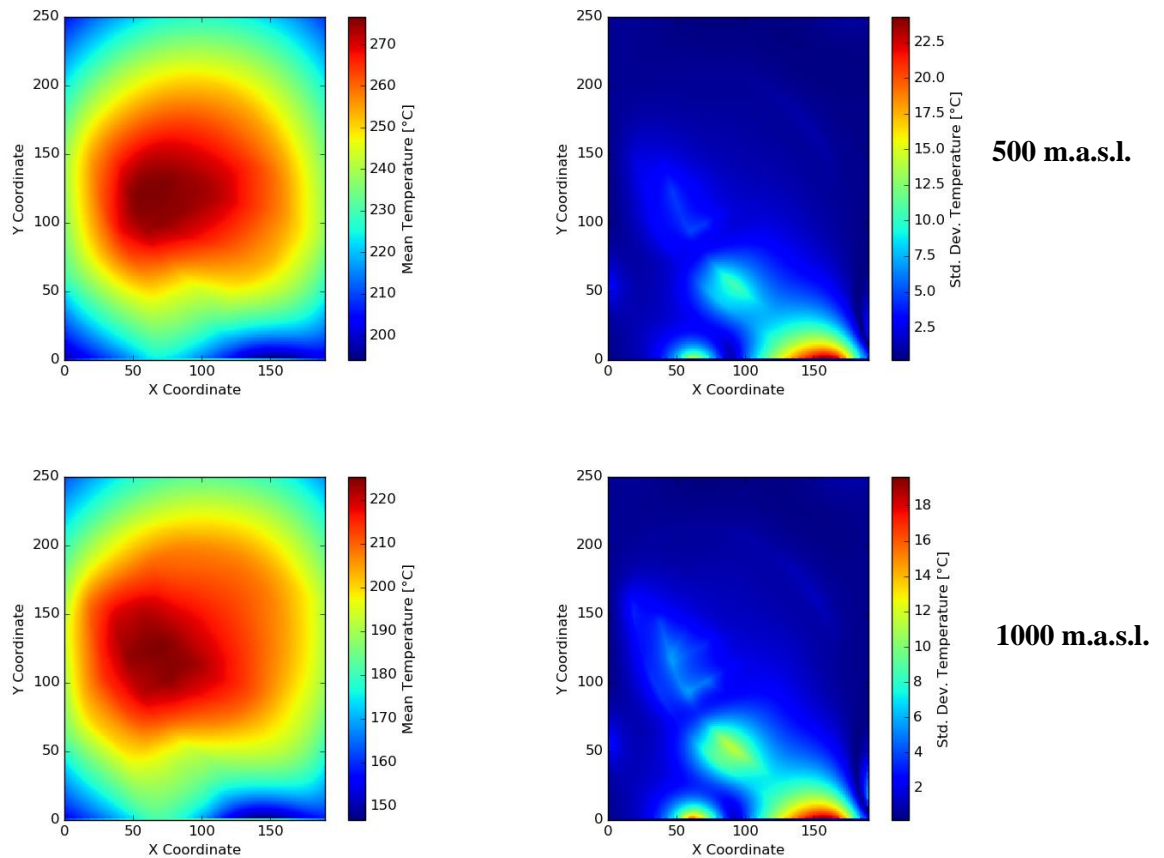


Figure 1.10: Mean temperature distribution (left) and standard deviation (right) extracted at 500 masl (top) and 1000 m.a.s.l. (bottom) within the reservoir model boundary obtained by staggering temperature fields from total 18 realisations (three different fault permeability scenarios simulated using six different boundary conditions)

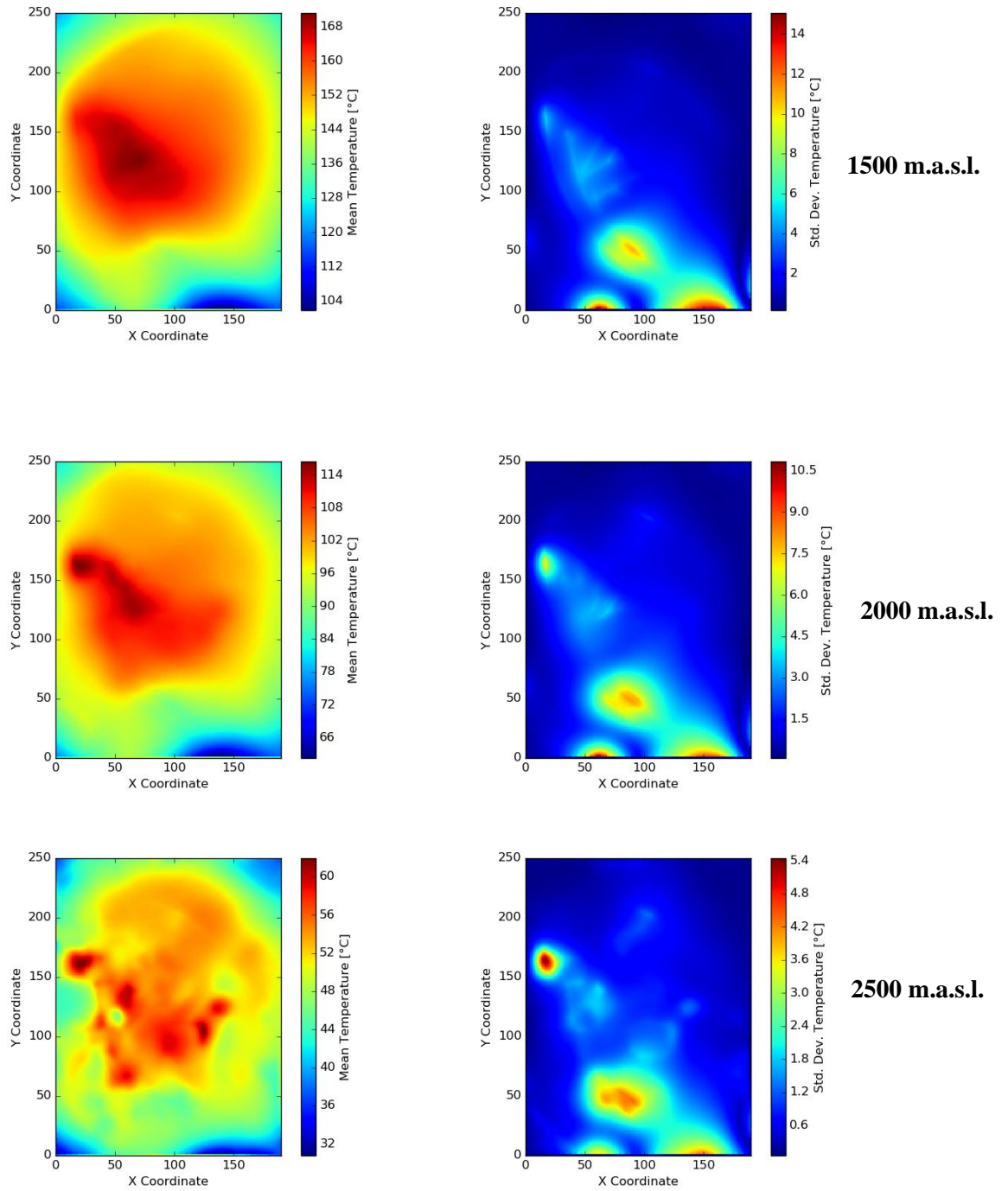


Figure 1.11: Mean temperature distribution (left) and standard deviation (right) extracted at 1500 m.a.s.l. (top), 2000 m.a.s.l. (middle) and 2500 m.a.s.l. (bottom) within the reservoir model boundary obtained by staggering temperature fields from total 18 realisations (three different fault permeability scenarios simulated using six different boundary conditions)

In deeper depths (500 m.a.s.l.) the temperature increase due to advection along the faults and is not that significantly pronounced as in shallower depths (e.g. 1500 m.a.s.l.). It can also be observed that the standard deviation in temperature decreases as we proceed towards shallow levels. The larger uncertainty in the

temperature prediction between different models at deeper depths is a result of increased advective heat transport in faults at the deeper levels in andesite and limestone, while at the shallower levels, the presence of the sealing ignimbrites inhibits the flow to a certain extent leading to very small differences in temperature for different structural configurations.

Figure 1.12 is a temperature map at 1000 m.a.s.l. with different well locations to show the overall result of different simulation runs. The black dots are well locations where the simulated temperature shows a good match with the bottom hole corrected temperature data, the well locations indicated in white are the locations where the simulated temperature is underestimated, while the locations indicated in yellow are overestimated in simulation.

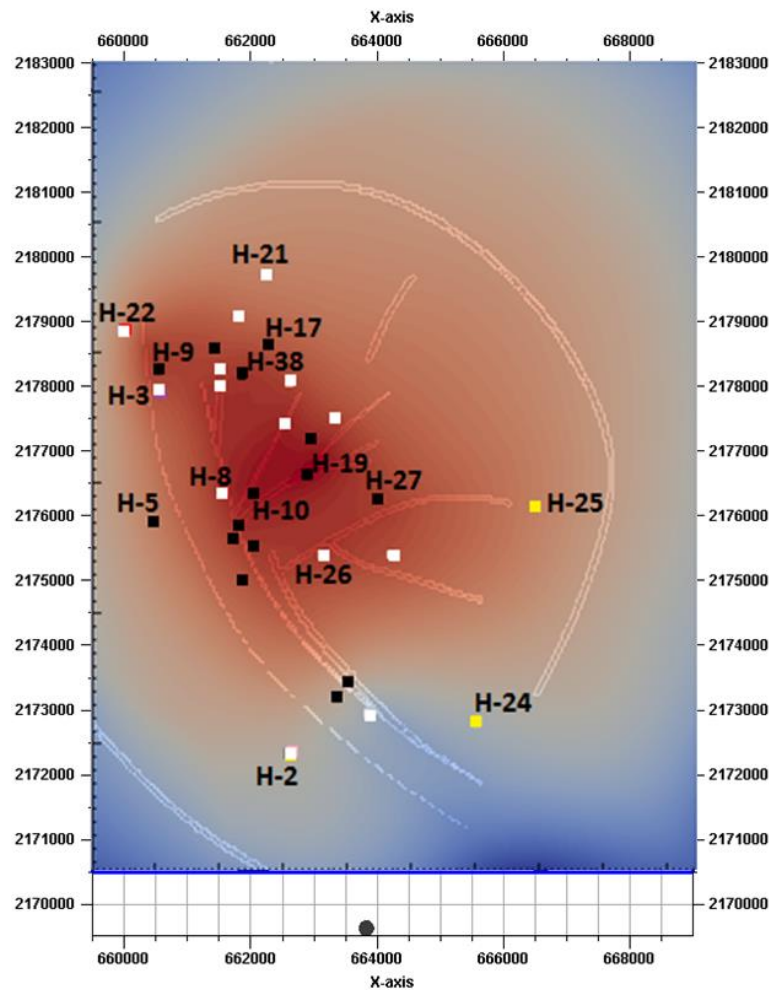


Figure 1.12: Mean temperature map extracted at 1000 m.a.s.l. showing well positions in different colors to indicate the overall match of the simulated temperature with bottomhole corrected temperature of wells, the black dots are well locations where the simulated temperature shows a good match with the bottom hole corrected temperature data, the well locations indicated in white and yellow show a mismatch of 30 °C – 50 °C

In Figures 1.13 – 1.15, we compare the simulated temperatures from all reservoir model variations for some well locations with the bottom hole corrected temperature of the respective well. The comparison of bottom-hole temperatures with the simulated temperatures matches well for many wells, some of them are shown here (Figure 1.13), while Figure 1.14 shows wells where the mismatch is greater than 30 °C and Figure 1.15 shows some wells where the simulation underestimates the temperature encountered by the wells.

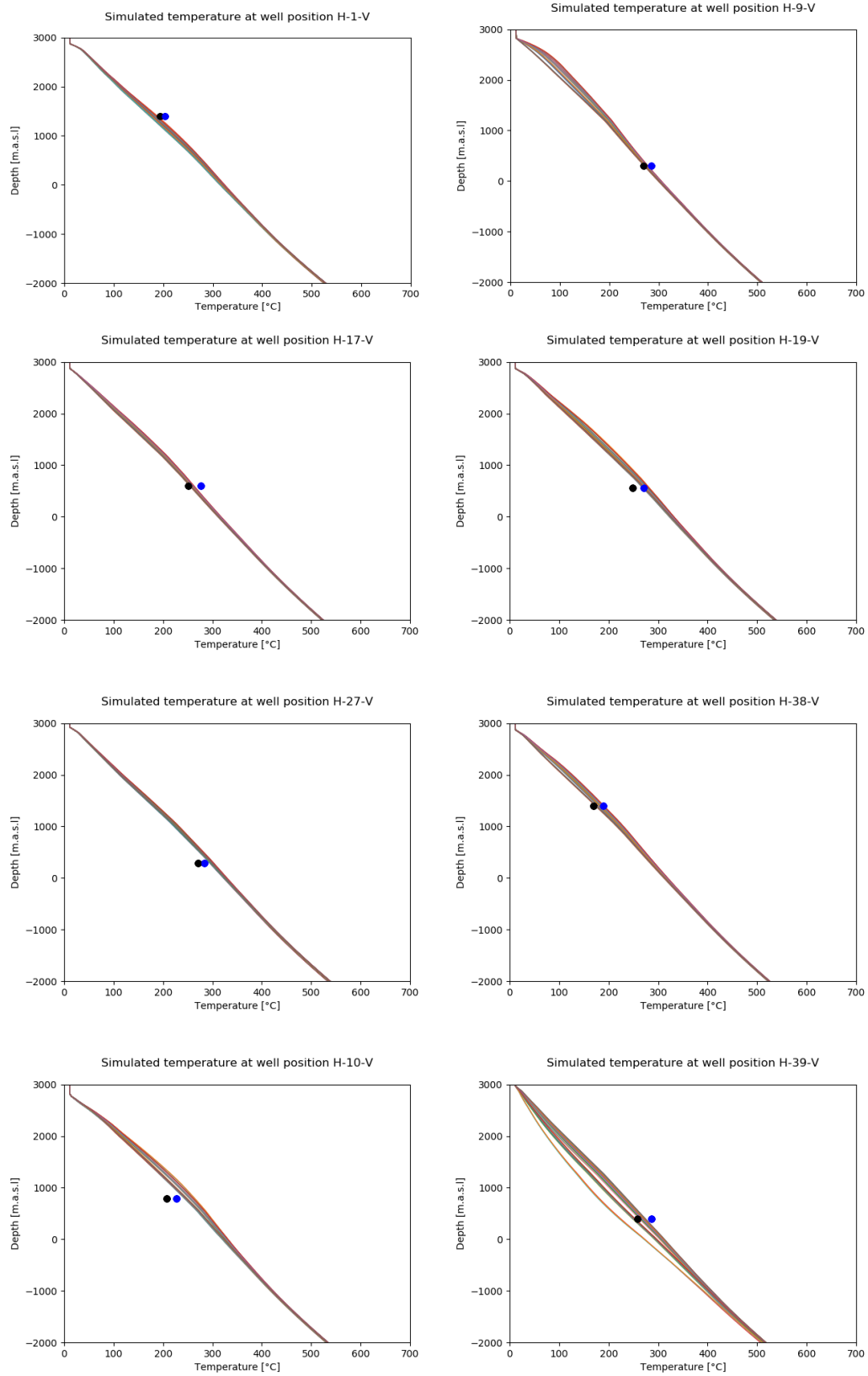


Figure 1.13: Good match between BHT for different well positions (black point - Horner corrected, blue point -spherical corrected BHT) and temperature extracted along respective well positions for different realisations indicated by colored lines.

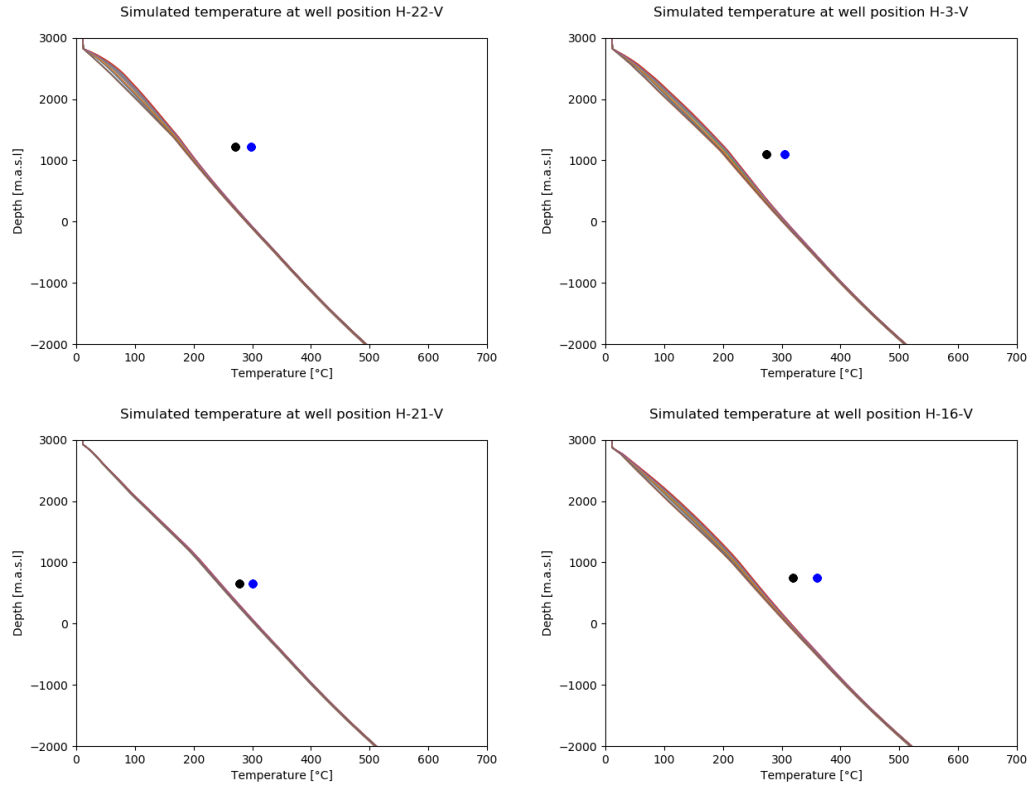


Figure 1.14: Mismatch between BHT for some well positions (black point - Horner corrected, blue point - spherical corrected BHT) and temperature extracted along respective well positions for different realisations indicated by colored lines

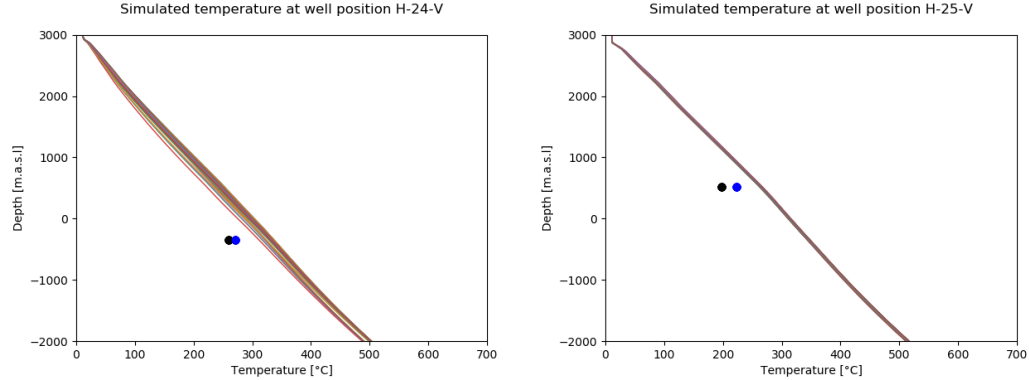


Figure 1.15: Overestimated BHT temperatures for wells H-24 and H-25 (black point - Horner corrected, blue point -spherical corrected BHT) and temperature extracted along respective well positions for different realisations indicated by colored lines

1.8 Conclusion and discussion

We simulated for the Los Humeros Caldera geothermal field steady state fluid flow and heat transport under natural conditions (i. e. prior to production) with particular focus on the permeability of the various fault systems. The structural model includes the main lithological units and explicitly comprises the major fault systems as structural units. Firstly we studied the field on a regional scale in an extent of 36 km NS to 56 km EW with vertical extent of 9.6 km. This was done to obtain an overview of the large scale flow and heat transport and to provide proper boundary conditions for a smaller reservoir model of size 12.5 km NS to 9.5 km EW with vertical extent of 6.5 km of which 3.0 km depth is below the mean sea level.

The steady state modeling results are strongly affected by the structural elements modelled in the field. This study is based on a preliminary structural model. The formations modelled in the structural model are based only on well data and lacks information from field scale geophysical data. This results in strong uncertainty in positions away from the wells. In addition, the depth and orientation of the local faults as well as the configuration of the main caldera rims are inferred based on superficial observations and are unfortunately not yet validated by geophysical data. Unclear fault sealing conditions adds to the above conditions leading to uncertainty in recharge and circulation through the caldera rims.

To address these questions related to structural uncertainties, we performed simulations to evaluate the effect of unknown configuration of the structural elements. Each of the scenarios summarised in local model are run with six different boundary conditions obtained from the regional scale modeling which addresses the uncertainty which could be due to the sealing condition of the major caldera faults. We further performed simulations varying the permeability of the local faults to evaluate the effect of permeability change in the temperature distribution at reservoir depth. The highest uncertainty of the temperature field is seen along the southern border of the local model as well as the NW-SE trending faults. These strong temperature differences are a result of combined effect of sealing conditions of Los Humeros Caldera rim fault (incorporated through the boundary conditions) and the corresponding temperature and pressure differences arising as a result of varying fault permeability values. The very hot temperature zones are observed in the middle and towards the north-western section of the reservoir model.

The heat zone distribution observed in the temperature maps reflects the chosen heat source configuration as boundary condition. We began our investigation with minimum knowledge of heat source distribution. Using different strengths of heat source and varying permeability conditions, it was not possible to match all the temperature observed in the wells of Los Humeros field. Comparing the simulated temperature with the bottom-hole corrected temperature, we observe that there is no obvious reason as to why certain wells show very good match while certain others do not. Along the faults especially, there are wells which are located just a few hundred meters away from each other, where one shows a perfect match with the simulation while the other is more than 30 °C off from the observed BHT. For example wells H-9 and H-3 or wells H-10 and H-8 (Figure 1.12) are both very close to each other, but H-9 and H-10 show a very good match with the simulated temperatures, whereas well H-3 and H-8 are underestimated in the simulations. Extremely hot wells in the north-western part of Los Humeros field (example H-22, H-3, etc.,) could not be matched with fault permeability of $5 \times 10^{-15} \text{ m}^2$. It is possible that the fault permeability considered in the simulations are relatively low and can be much higher in magnitude depending on the extent of the fault affected zone or much lower in case of extended precipitation of minerals in the pathways. The figures are however an indicative of the fault permeability related impact on the temperature distribution.

In the north-western part of the Los Humeros geothermal field, the simulated temperature is underestimated for several wells. As mentioned probably the permeability of the faults in these areas are greater than $5 \times 10^{-15} \text{ m}^2$ which could not be modelled due to numerical instability. However, it is also possible that the basal heat flux in these zones are stronger than the value used for simulation. The hot zones could be created due to the presence of much shallower local intrusions in the north-western part of the field. This hypothesis needs to be verified using other data sources such as seismic or resistivity data. Further numerical modeling in this area should be performed using more information confirming the heat source and improved structural model.

1.9 References

- Aragón, A., Moya, S.L., García-Gutiérrez, A., Arrelano, V., 2008. A new method of damage determination in geothermal wells from geothermal inflow with application to Los Humeros, Mexico. *Geofísica Internacional*, 47(4), 371 – 382.
- Arrelano, V. M., García, R.M., Barragán, G., Izquierdo, A., Araagón, A., Nieva, D., 2003. An updated conceptual model of the Los Humeros geothermal reservoir (Mexico), *Journal of Volcanology and Geothermal Reserarch*, 124, 67- 88.
- Arellano, V. M., Barragán, R. M., Ramírez, M., López, S., Paredes, A., Aragón, A., Tovar, R., 2015. The Response to Exploitation of the Los Humeros (México) Geothermal Reservoir. *Proceedings World Geothermal Congress 2015, Melbourne, Australia*.
- [Ascencio, F., Garcia, A., Rivera, J. and Arellano, V., 1994. Estimation of undisturbed formation temperatures under spherical-radial heat flow conditions. *Geothermics*, 23, 4, 317-326.
- Campos-Enríquez, J. O., Arredondo-Fragoso, J. J., 1992. Gravity study of Los Humeros caldera complex, Mexico: Structure and associated geothermal system, *Journal of Volcanology and Geothermal Reserarch*, 49, 69 – 90.
- Calcagno, P., Evanno, g., Trumpy, E., Gutiérrez-Negrín, L. C., Macías, J. L., Carrasco-Núñez, G., Liotta, D., 2018. Preliminary 3-D geological models of Los Humeros and Acoculco geothermal fields (Mexico) – H2020 GEMex Project., *Advances in Geosciences*, 45, 321 – 333.
- Carrasco-Núñez, G., López-Martínez, M., Hernández, J., Vargas, V., 2017. Subsurface stratigraphy and its correlation with the surficial geology at Los Humeros geothermal field, eastern Trans-Mexican Volcanic Belt, *Geothermics*, 67, 1 – 17.
- Cedillo-Rodríguez, F, 2000. Hydrogeologic model of the geothermal reservoirs from Los Humeros, Puebla, Mexico. *Proceedings World Geothermal Congress 2000, Kyushu – Tohoku, Japan, May 28 – June 10, 2000*.
- Estudio geohidrológico C.G. Los Humeros, 2015, CFE
- Clauser, C., 1984. A climatic correction on temperature gradients using surface temperature series of various periods. *Tectonophysics*, 103, 33 – 46.
- Clauser, C., 1992. Permeability of crystalline rocks. *EOS, Transactions American Geophysical Union*, (73), 233 – 238.
- Clauser, C., ed., 2003. *Numerical Simulation of Reactive Flow in Hot Aquifers. SHEMAT and PROCESSING SHEMAT*, Springer, New York.
- Clauser, C., 2011a. Thermal Storage and Transport Properties of Rocks, II: Heat Capacity and Latent Heat, In: Gupta, H. (ed.), *Encyclopedia of Solid Earth Geophysics*, Springer, Berlin.
- Clauser, C., 2011b. Thermal Storage and Transport Properties of Rocks, II: Thermal Conductivity and Diffusivity, In: Gupta, H. (ed.), *Encyclopedia of Solid Earth Geophysics*, Springer, Berlin.
- Davies, J. H., 2013. Global map of solid Earth surface heat flow. *Geochem. Geophys. Geosyst.*, 14, 4608 – 4622.

- de Marsily, G., 1986. *Quantitative Hydrogeology: Groundwater Hydrology for Engineers*. Academic Press.
- Dowdle, W. L. and Cobb, W.M., 1975. Static formation temperature from well logs – an empirical method, *Journal of Petroleum Technology* 27 (11), 1326-1330
- Evans, J. P., Forster, C. B., Goddard, J. V., 1997. Permeability of fault-related rocks, and implications for hydraulic structure of fault zones, *Journal of Structural Geology*, 19(11), 1397 – 1404.
- Eppelbaum, L.V. and Kutasov, I.M., 2006. Determination of formation temperatures from temperature logs in deep boreholes: comparison of three methods, *Journal of Geophysics and Engineering*, 348 – 355.
- Ferriz, H. and Mahood, G.A. 1984. Eruption rates and compositional trends at Los Hornos Volcanic Center, Puebla, Mexico. *Journal of Geophysical Research* 89(B10), 8511 – 8524, doi: 10.1029/JB080i010p08511.
- García-Gutiérrez, A., Arellano, V., Barragán, R.M. Espinosa-Paredes, G. 2002, Initial temperature field in the Los Hornos geothermal reservoir, *Geofísica Internacional*, 41, 3, 303-312.
- García-Palomo, A., Macías, J. L., Tolson, G., Valdez, G., Mora, J. C., 2002. Volcanic stratigraphy and geological evolution of the Apan region, east central sector of the Trans-Mexican Volcanic Belt. *Geofísica Internacional*, 41(2), 133 – 150.
- Giordano G., Lucci F., Rossetti F., Urbani S. 2018. Update on the volcanological conceptual model of Los Hornos geothermal field, *3rd GEMex Meeting, Morelia*
- Hartmann, A., Rath, V., Clauser, C., 2005. Thermal conductivity from core and well log data. *International Journal of Rock and Mechanics & Mining Sciences*, 42, 1042 – 1055.
- Heap, M. J., Kennedy, B. M., Exploring the scale-dependent permeability of fractured andesite. *Earth and Planetary Science Letters*, 447, 139 – 150.
- Horner D. R., 1951. Pressure buildup in wells, in Proceedings of Third World Petroleum Congress, Section II, The Hague, Netherlands, 28 May – 6 June.
- Norini, G., Groppelli, G., Sulpizio, R., Carrasco-Núñez, G., Dávila-Harris, P., Pelliccioli, C., Zucca, F., De Franco, R., 2015. Structural analysis and thermal remote sensing of the Los Hornos Volcanic Complex: Implications for volcano structure and geothermal exploration. *Journal of Volcanology and Geothermal Research*, 301, 221 – 237.
- Lee, Y., Deming, D., 1998. Evaluation of thermal conductivity temperature corrections applied in terrestrial heat flow studies. *Journal of Geophysical Research*, 103(B2), 2447 – 2454.
- Lopez-Hernandez, A., 1995. Estudio Regional Volcanico y Estructural del Campo Geotermico de Los Hornos, Pue., Mexico. *Geoterm. Rev. Mex. Geoenerg.* 11 (1), 17–36.
- Pardó M., Suárez, G., 1995. Shape of the subducted Rivera and Cocos plates in southern Mexico: Seismic and tectonic implications. *Journal of Geophysical Research*, 100(B7), 12357 – 12373; doi:10.1029/95JB00919.
- Pasquale, V., Verdoya, M., Chiozzi, P., 2017. *Geothermics Heat Flow in the Lithosphere*, 2nd edition, SpringerBriefs in Earth Sciences, Cham, Switzerland. doi: 10.1007/978-3-319-52084-1

- Pollack, H. N., Hurter, S. J., Johnson, J., R., 2010. Heat flow from the earth's interior: Analysis of the global data set. *Review of Geophysics*, 31, 267-280.
- Pulido, C. D. L., 2008. Borehole Geophysics and Geology of well H-43, Los Humeros Geothermal Field, Puebla, México. *Geothermal Training Programme Report*, 23 (2008), *Orkustofnun, Grensásvegur 9, IS-108 Reykjavík, Iceland*
- Rath, V., Wolf, A., Bücker, M., 2006. Joint three-dimensional inversion of coupled groundwater flow and heat transfer based on automatic differentiation: sensitivity, calculation, verification, and synthetic examples, *Geophys. J. Int.*, 167, 453 – 466.
- Roure, F., Alzaga-Ruiz, H., Callot, J.-P., Ferket, H., Granjeon, D., Gonzalez-Mercado, G. E., Guilhaumou, N., Lopez, M., Mougín, P., Ortuno-Arzate, S., Séranne, M., 2009. Long lasting interactions between tectonic loading, unroofing, post-rift thermal subsidence and sedimentary transfers along the western margin of the Gulf of Mexico: Some insights from integrated quantitative studies, *Tectonophysics*, 475, 169 – 189.
- Rybach, L., 1976. Radioactive Heat Production: A Physical Property Determined by the Chemistry of Rocks, In: Strens, R. G. J. (ed.), *The Physics and Chemistry of Minerals and Rocks*, 309 – 318, Wiley & Sons, London
- Rybach, L., 1986. Amount and Significance of Radioactive Heat Sources in Sediments, In: Burrus, J. (ed.), *Thermal Modelling in Sedimentary Basins*, Editions Technip, 311-322.
- Sánchez Luviano, M., Armenta, M. F., Montes, M. R., 2015. Thermal Stimulation to Improve the Permeability of Geothermal Wells in Los Humeros Geothermal Field, Mexico. *Proceedings World Geothermal Congress 2015, Melbourne, Australia*.
- Schön, J. H., 2004. *Physical Properties of Rocks: Fundamentals and Principles of Petrophysics*, 1. Edition, Elsevier, Amsterdam.
- Sekiguchi, K., 1984. A method for determining terrestrial heat flow in oil basin areas. *Tectonophysics*, 103, 67 – 79, Elsevier Science Publishers B. V. Amsterdam – Netherlands.
- Smerdon, J. E., und Stieglitz, M., 2006. Simulating heat transport of harmonic temperature signals in the Earth's shallow subsurface: Lower boundary of sensitivities, *Geophys. Res. Lett.*, 33, L14402, doi: 10.1029/2006GL026816.
- Suter, M., 1984. Cordilleran deformation along the eastern edge of the Calles-San Luis Potosí carbonate platform, Sierra Madre Oriental fold thrust belt, east-central Mexico. *Geological Society of America Bulletin*, 95, 1387 – 1397.
- Verma, S. P., 1985. Heat source in Los Humeros geothermal area, Puebla, Mexico. *Transactions of the Geothermal Resource Council*, 9, 521 – 525.
- Verma, S. P., Gómez-Arias, E., & Andaverde, J. (2011). Thermal sensitivity analysis of emplacement of the magma chamber in Los Humeros caldera, Puebla, Mexico. *International Geology Review*, 53(8), 905-925.
- Wagner, W., Cooper, J., Dittmann, A., Kijima, J., Kretzschmar, H., Kruse, A., Mares, R., Oguchi, K., Sato, H., Stocker, I., Sifner, O., Takaishi, Y., Tanishita, I., Trubenbach, J., Willkommen, T., 2000. The IAPWS industrial formulation 1997 for the thermodynamic properties of water and steam. *J Eng Gas Turbines Power Trans ASME*. 2000, 122(1), 150–82. doi:10.1115/1.483186.

Ziagos, J. P., Blackwell, D. D., Mooser, F., 1985. Heat Flow in Southern Mexico and the Thermal Effects of Subduction. *Journal of Geophysical Research*, 90, 5410 – 5420.

Zoth, G., Hänel, R., 1988. Appendix: 10.1. Thermal Conductivity. In: Hänel, R., Rybach, L., Stegna, L., (eds.), Handbook of terrestrial heat flow density determination, Kluwer Academic Publishers, Dordrecht, pp 447 – 468.

2 PART 2 – CNR

(Giordano Montegrossi)

2.1 Introduction

In this report, we describe an alternate approach towards simulation of Los Humeros geothermal field. The results of the CFE confidential data analysis, related to reservoir engineering for task 6.2 create a conceptual static reservoir model parametrization used for steady state (natural state) 3D numerical model of Los Humeros geothermal system in tasks 6.4.

A 3D model representation and visualization combines results from characterizing, exploring, and modelling the required physical properties at in situ reservoir conditions. The work consists of:

- 1) Investigation on heating up profile, to identify the possible feed zones
- 2) Investigation on pressure build up during heating, to identify the pivot point and the pressure controlling the feed zones as well as the pressure in the wellbore surrounding
- 3) Wellbore modeling to assess fluid P,T, enthalpy and phase segregation along well profile.

This approach was followed for each well, according to the availability of the needed data in the data package provided by CFE.

Once the field data, consisting of well log data and results from other tasks are elaborated, we define the petrophysical properties of the rocks and the boundary condition of the model using the available data and results properly accounted all along the report.

A numerical model of the Los Humeros steady state (natural state) will be set up by defining the boundary conditions and repeatedly running the model until a satisfactory calibration against field data is obtained, and the model results are shown in section 9.3 and 9.4 of the report, with the calibration results.

2.2 Objective

The present report deal with the use and the refinement of state-of-the-art simulation codes (i.e. TOUGH2 with Equation of State for supercritical water and CO₂) applied by contributing partners for generating a model for the super-hot reservoir at Los Humeros and its calibration against available field data.

The model comprise explicit or adequately parameterised fractured/permeable zones within the reservoir rocks, and provide a structure of the reservoir/permeable zones.

Results of the numerical model of the natural state of the system and thermal regimes will be reported, with uncertainty estimates of the model predictions caused by uncertainty in model input parameters or calibration data.

2.3 Data Available

2.3.1 Reservoir engineering: feed zones, temperature and pivot point

The data used for the present work were provided by CFE, and consist mainly of temperature and pressure logs during heating up and production data. These field data were then elaborated as described below, according to normal interpretation for geothermal systems (Grant and Bixley, 2011), to obtain the needed information for the numerical modeling.

The temperature profiles while heating up are commonly seen in wells just after drilling or after cold water injection. Some temperature peaks can be seen and suggest permeable feed zones, but the permeability is not high enough to cause a massive flow between feed zones. It is commonly found that the bottom of the well is very undisturbed, which causes the high temperature gradient.

After drilling, the borehole is closed and given time to recover. After some time has passed, the temperature recovery is measured and then the hole is closed again. This is repeated several times, and the temperature build-up measurements are then used to interpret the formation temperature around the well. A spinner log would help in assessing fluid flow during static logs.

In this work the feed zones are treated as permeable reservoir zones that, in the well surrounding, provide a preferential heating up of the well due to the more efficient heat transfer in presence of fluids with respect to the rock conductivity. Thus, the feed zones evidenced with this procedure may not be coincident with the productive zones of the well, because of well completion and preferential fluid flow path in fracture surrounding the well. The latter effect is generally more relevant for systems with vertical fractures. The last remark is on the deep reservoir bottom: since the deepest feed zone often hit the well bottom, its positioning is limited by the drilled depth. We can more clearly observe this effect in the flowing well temperature profiles (dynamic logs), that in many cases seems to not be properly flowing at the level of the deep feed zones, thus suggesting a lower limit to the local producing zone (to be differentiated from the feed zone).

After investigating the temperature profiles while heating up, we proceed to work on pressure profiles while heating up.

2.3.2 Temperature log interpretation

A typical example of the heating up profile with dynamic log, with feed zones defined by “thermal fingers” is reported in Figure 2.1. In this example, the well H-49, central area, is considered. The heating up profiles with the shallow and deep feed zones are evidenced; from the upper and lower boundary of the heating up figure we can obtain the positioning of the shallow and deep feed zones, and the extrapolated temperature for both feed zones as well. In figure 2.1, the Flowing Well temperature log (Dynamic log) is shown, and a non-flowing zone at the level of deep feed zone could be observed. In this case, the temperature of the dynamic log (flowing section) could be clearly related to the temperature of the shallow feed zone. This procedure is then repeated for all the available wells, correcting the depth from measured depth to True Vertical Depth (TVD) in case of deviated wells, and the results are reported in table 2.1.

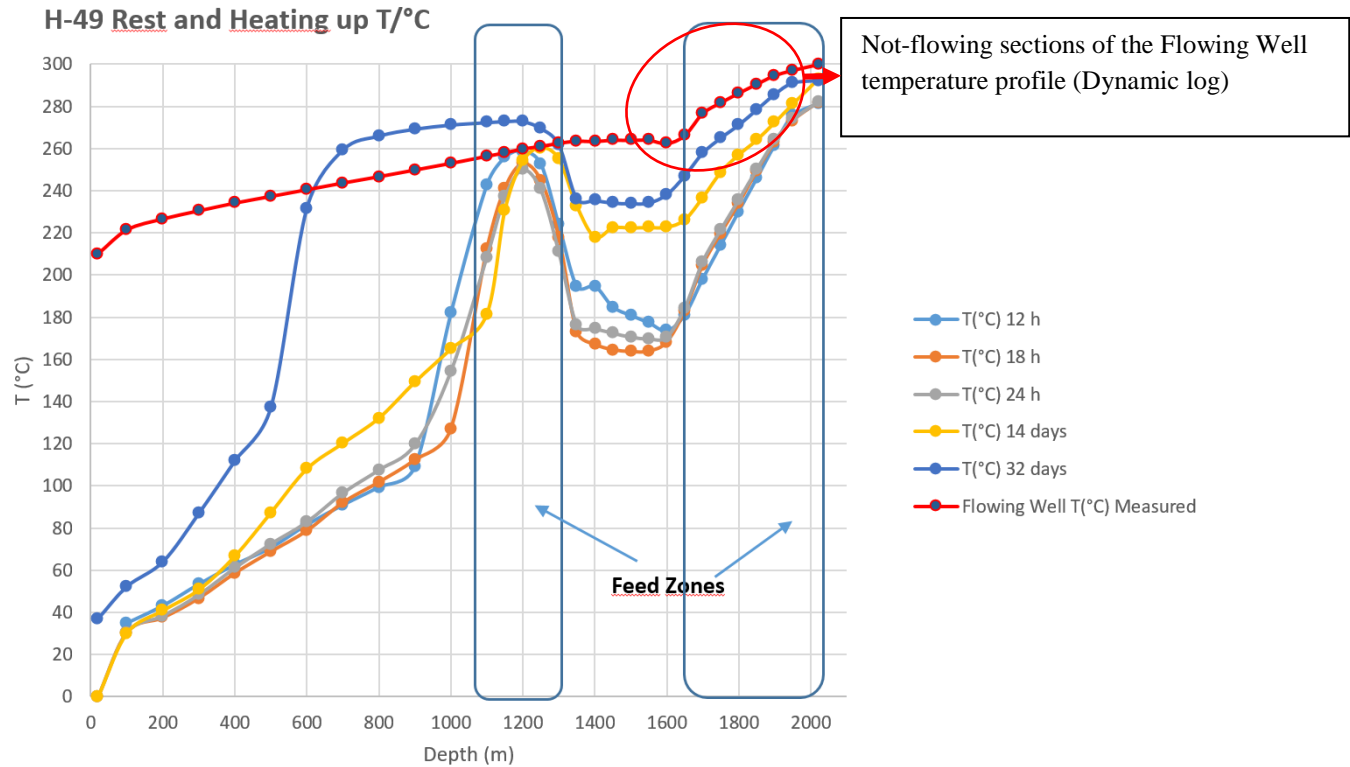


Figure 2.1: Well H-49, central area. Here is an example of heating up profiles with the shallow and deep feed zones evidenced. In the figure, the Flowing Well temperature log (Dynamic log) is shown, and a non-flowing zone at the level of deep feed zone could be observed. In this case, the temperature of the dynamic log (flowing section) could be clearly related to the temperature of the shallow feed zone

2.3.3 Pressure log interpretation

After shut-in, the well pressure slowly reaches an equilibrium with the pressure distribution in the geothermal reservoir. During this time, the pressure profiles measured in the well typically pivot about a fixed point called the pivot point. This is because, during heating up the water density change, the corresponding pressure profile change, up to boiling and forming a counter pressure against the closed well-head. If no external control is present, the pressure profiles in time is made up by many non-intersecting curves, while if an external control is present the pressure profiles during heating up intersect and move around a common Pivot point. Generally speaking, if the well has a single feed zone, the pivot point is located at the depth of that feed zone, whereas if the well has several feed zones the pivot point should be located between these. The pressure of the pivot point is essentially controlled by the main alimentation of the reservoir that could be the recharge or could be related to the fluid mass distribution along the feed zones.

Therefore, the Pivot point gives solid information on the pressure of the reservoir at that depth. An example of Pivot point for well H-49 could be observed in Figure 2.2. In this case, compared to the temperature heating up profiles, the Pivot point is located slightly below the first feed zone.

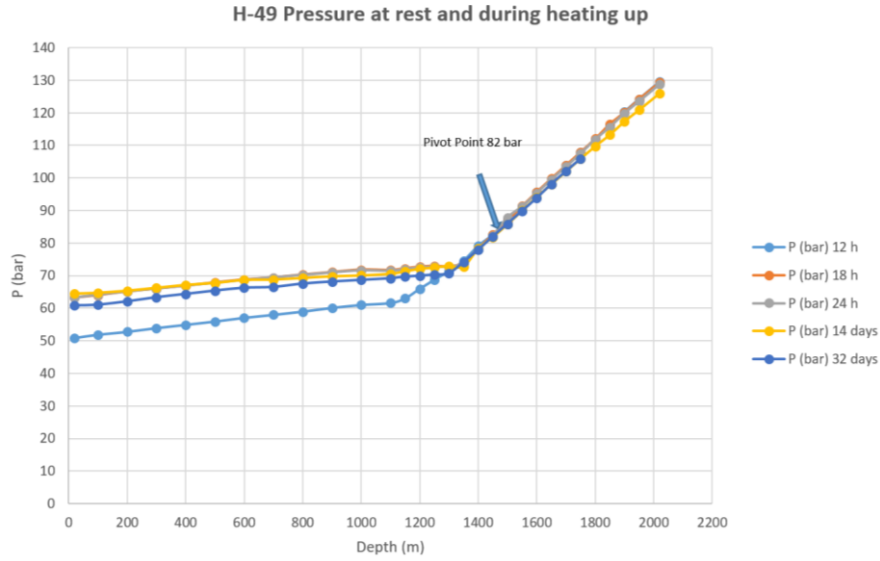


Figure 2.2: Well H-49, central area. Pressure profiles during heating up show a steam zone (nearly 0-1300 m depth), and a liquid zone, in which a Pivot point could be observed at 1450 m depth with 82 bar.

2.3.4 Results of temperature and pressure log interpretation

As a result of the investigation of temperature and pressure logs, we were able to identify the position of feed zones in most of the available wells. Usually, two feed zones are found, but in some wells we could only identify one and in some other we could found up to 3 feed zones. For each identified feed zone, we assigned (if possible) the corresponding temperature, and we reported the pivot point pressure and depth; all the results from the present investigation are reported in table 2.1.

Table 2.1: Results from well logs investigation, feed zones position and temperature with pivot point position and pressure

Well	Coordinates		Elevation (masl)	Depth (m)	Coordinates Well Bottom		1st feed zone		Pivot point		2nd feed zone		3rd feed zone		Notes			
	UTM X	UTM Y	TOP		UTM X	UTM Y	TVD (masl)	Top(masl)	Bottom(masl)	T (°C)	Elevation (masl)	Pressure (bar)	Top(masl)	Bottom (masl)	T (°C)	Top(masl)	Bottom(masl)	T (°C)
H-1V	661906	2175064	2828	1850	661906	2175064	978	1728	1428	270			2828	2828				
H-10D	661906	2175064	2828	1800	661906	2175035	1028	1728	1428	250			1228	1028	287			Deviated
H-2	662466	2172435	2896	2304	662466	2172435	592	2896	2896				1096	596	331			
H-3V	660622	2177933	2735	1680	660622	2177933	1075	1455	1305	200			1205	1059	315			
H-30	660622	2177933	2735	1860	660979	2177762	1796	1755	1555	205			1455	1069	290			Deviated
H-5	660540	2175950	2762	1905	660540	2175950	857	1662	1462				1012	917				
H-6-V	663508	2173545	2894	2540	663508	2173545	354	2894	2894				982	782	237	632		
H-7-V	661838	2175671	2782	2300	661838	2175671	482	1582	1382	214	982	123	571	401	362			273.5
H-8-V	661582	2176392	2771	2200	661582	2176392	471	1243	1066	236	971	124	402	302				
H-9-V	660618	2178216	2752	2500	660618	2178216	252	952	652				134					
H-10-V	662081	2176381	2838	2100	662081	2176381	738	1162	1063				860	697	224			
H-11-V	662574	2177436	2812	2300	662574	2177436	512	2812	2812		1662	97			354			Deviated
H-11D	662574	2177436	2812	1400	662468	2177463	1412	1612	1347	318	1532	102						
H-12	663803	2173053	2973	3104	663803	2173053	-131	1573	1323	274	1448	114	323	-11	351			
H-13-V	662244	2177406	2835	2400	662244	2177406	435	1235	1135	171	1185	112.2	735	635	220	535		434
H-13D	662244	2177406	2835	2300	662460	2174692	535	1385	1185	196	1485	82.7	1110	1010	254			Deviated
H-15-V	661638	2178804	2795	1973	661638	2178804	822	1595	1395	216	1345	116						
H-15D	661638	2178804	2795	1502	661640	2178850	1293	1695	1332	295								Deviated
H-16-V	661557	2178250	2783	2038	661557	2178250	745	1588	1333	212			944	745	344			
H-17-V	662298	2178606	2813	2265	662298	2178606	548	1413	1313	198	1613	99	863	599	329.1			Deviated
H-17D	662298	2178606	2813	1700	662115	2178634	1113	1393	1143	302	1163	133.8						Deviated
H-18-V	660916	2172077	3002	2900	664916	2172077	102	1352	1252	168	1332	162	552	143	348.2			
H-19-V	662881	2176643	2808	2270	662881	2176643	538	1779	1458	200	1508	115.1	858	558	320.2			
H-19D	662881	2176643	2808	1800	662950	2176661	1008	2808	2808									Deviated
H-20-V	663330	2177486	2830	2400	663330	2177486	430	1430	1130	186	1430	105	680	435	271.2			
H-21-V	662279	2179691	2871	2200	662279	2179691	671	971	871		1071	135	771	657				
H-22	660055	2178853	2770	1546	660055	2178853	1224	1970	1820	131	1895	80	520	1231	245			
H-23	664184	2175459	2872	2620	664184	2175459	252	1272	972	200				267	350			
H-24	665497	2172938	2949	3280.6	665497	2172938	-331.6	1049	749	164								
H-25-V	666393	2176169	2800	2200	666393	2176169	500	1000	517	173								
H-26	663133	2175639	2876	2546	663133	2175639	330	1076	876	201			576	346	341			
H-27	663986	2176292	2870	2600	663986	2176292	270	1470	1270	185	1370	97	1020	820	210	420		254
H-28	663601	2177741	2820	2575	662601	2177741	245	1520	1020	230				262	361			
H-29D	661884	2177813	2817	2021.6	661877	2177845	785.4	1567	1317	299	1442	103	817	631	351			Injection
H-30-V	661488	2178547	2787	1900	661488	2178547	887	1337	1037	278.2	1337	113.3						
H-31-V	661832	2179041	2810	1926	661832	2179041	884	1410	1160	312.5	1210	126	960	885	339.2			
H-32-V	662631	2178043	2818	2202	662631	2178043	616	1618	1318	251.5	1368	113	718	632	306.8			
H-33-V	661534	2177986	2782	1600	661534	2177986	1182	1782	1532	281	1682	92	913	763				
H-34-V	662965	2177207	2813	1800	662965	2177207	1013	1463	1383	251.25	1563	93	1212	1142	306.9			
H-34D	662965	2177207	2813	2200	662965	2177207	613	1613	1313	173	1413	107						
H-37D	661074	2178346	2772	1798	660973	2178054	974	1485	1302	237.4	1372	117	445	295				Deviated
H-38-V	661897	2178155	2795	2200	661897	2178155	595	1786	1136	710	1395	113.6	710	590	219			Injection
H-39-V	663365	2173291	2890	2495	663365	2173291	395	1070	920	176.5	1240	102.5	887	795	296			
H-40D	661754	2175711	2795	2226	661546	2175655	569	1140	983	264	1030	111.2						Deviated
H-41	663570	2173280	2810	2200	663570	2173280	610	1510	1310	158			710	610	289			
H-42-V	661320	2173400	2890	2200	661320	2173400	690	1460	1390	286	1590	84	1338	1088	312			
H-43	661175	2178035	2780	2200	661175	2178035	580	1530	1230	206	1380	116	880	580	324			
H-44D	662534	2178347	2808	1170	662237	2178350	1038	1673	1523	205	1708	105	1030	530	321			Deviated
H-45D	661600	2176392	2780	2270	661729	2176373	510	1680	1380	168			982	862	308			Deviated
H-46-V	663021	2178288	2832	2000	663021	2178288	832	1432	1082	280	1232	108		813				
H-49D	662067	2175503	2798	2030	661946	2175602	768	1698	1248	203	1450	94			319			Deviated
H-49	661866	2175033	2825	2030	661877	2177845	817	1725	1475	254	1450	82	1175	805	300			Deviated
H-50D	663536	2173024	2937	2500	663801	2172938	437	1887	1567	275.3	1137	97	1260	1080	311			Deviated
H-52-V	661011	2178095	2760	1900	661011	2178095	860	1760	1560	284	1260	112	721	606	337			Deviated
H-55D	663331	2177648	2826	2282	663620	2177867	544	1151	961	314	966	120	754	609	338			Deviated
H-56	662238	2174382	2835	2380	661974	2174234	484.65	1685	1385	240	1535	116	1135	635	302			Deviated
H-58	662555	2177466	2804	2200	662555	2177456	604	1604	1354	265	1479	100	1304	1054	308	704		
H-59	661574	2178239	2804	2200	661574	2178239	604	1704	1404	250	1554	85	804	614	342			
H-64D	662590	2176499	2817	2300	662638	2176165	517	1517	1187	262	1187	103	821	354	317			Deviated

The pivot point pressure show a good correlation with depth (figure 2.3), clearly related to a common source/recharge. The recharge pressure is then modulated by the temperature distribution of the system, and the observed pressure gradient have a slope of 0.0445 bar/m that could be related to a hot hydrostatic pressure gradient.

The temperature distribution (Figure 2.4) does not have a very good correlation with depth, confirming that the heating up is not very homogeneous and possibly related to the presence of hot intrusions (and the relative possible boiling areas). The temperature vs depth correlations found so far could be used to initialize the model, that will be refined by including the correct position of the hot intrusions and both the natural (recharge) and induced (by means of reinjection and production) circulations.

The contrast between the highest temperatures and the average temperature found at the deep feed zone suggest that we are close to “the roots” of the geothermal system, with a relevant temperature spatial distribution. We can build a PT diagram (Figure 2.5) using the temperature of the feed zones and compute the corresponding pressure using the Pivot Point pressure and a local pressure gradient obtained on the temperature gradient basis. We may observe in figure 2.5 that generally the reservoirs are in the liquid field, and this is true for all the shallow feed zone and part of the deep ones. In particular, for the deep feed zone the P,T condition approach the boiling line and reach the vapour field, suggesting that there are boiling areas. These boiling areas could be linked to the presence of hot intrusions that are directly in contact with the circulating fluids, or to the effect of exploitation.

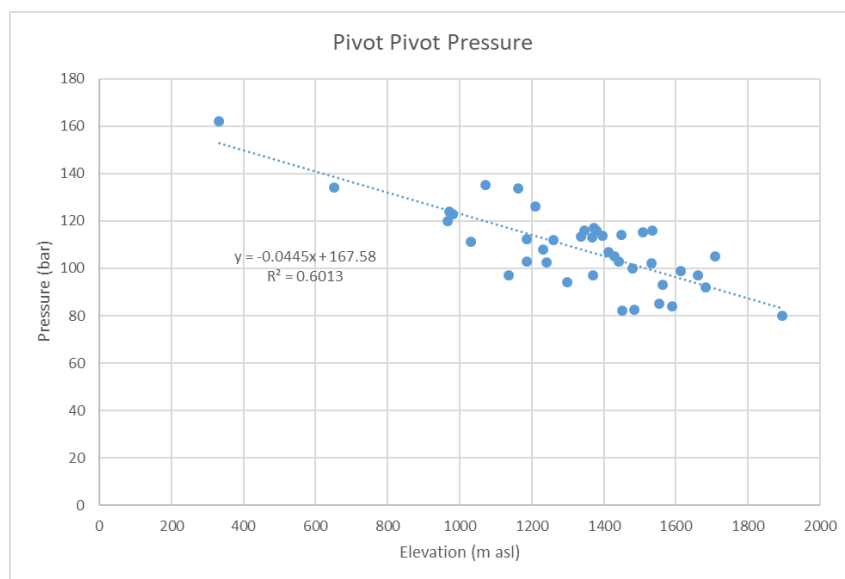


Figure 2.3: Pressure of Pivot point vs Depth

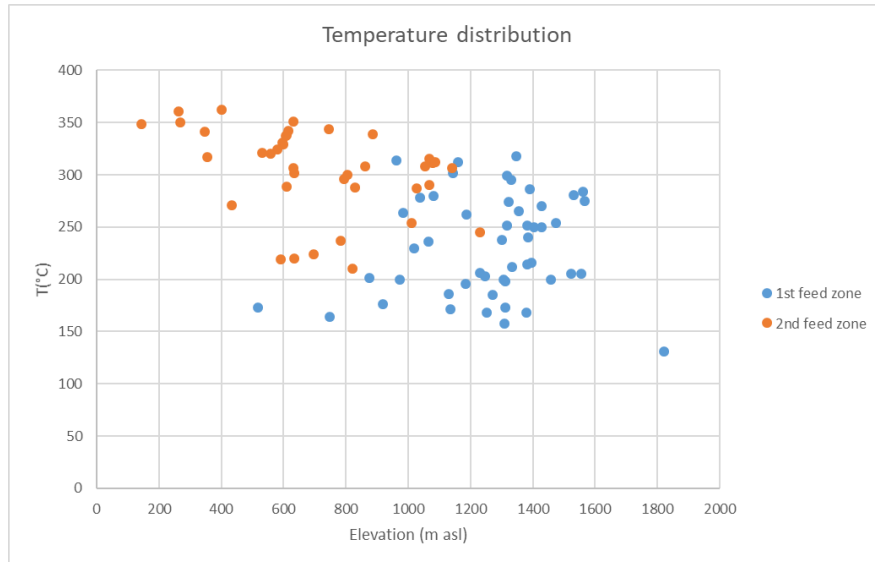


Figure 2.4: Temperature distribution vs Depth

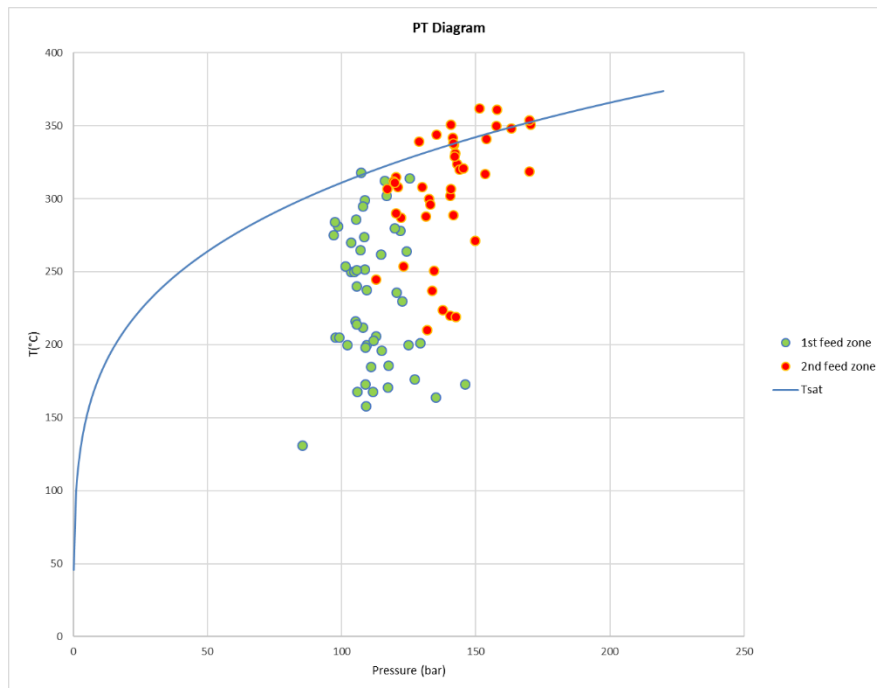


Figure 2.5: PT Diagram

2.4 Recharge path and water table

The diagram in figure 2.6, obtained using the isotope data from CFE and results of task 4.3, show that the recharge input is mainly related to the 1st feed zone, that have a large temperature span around 250 °C. The Isotope distribution, with boiling model, presented in task 4.3 and here reported in figure 2.6 show that the

recharge is likely due to regional input of water circulating in limestones. The recharge water enter in the Los Humeros geothermal system at temperature ranging 200 – 250 °C, and after that follow multiple step boiling (possibly interacting with the fluid in the deep feed zone) and mixing with reinjection, as reported in Figure 2.6 (stable isotope data are a courtesy of CFE).

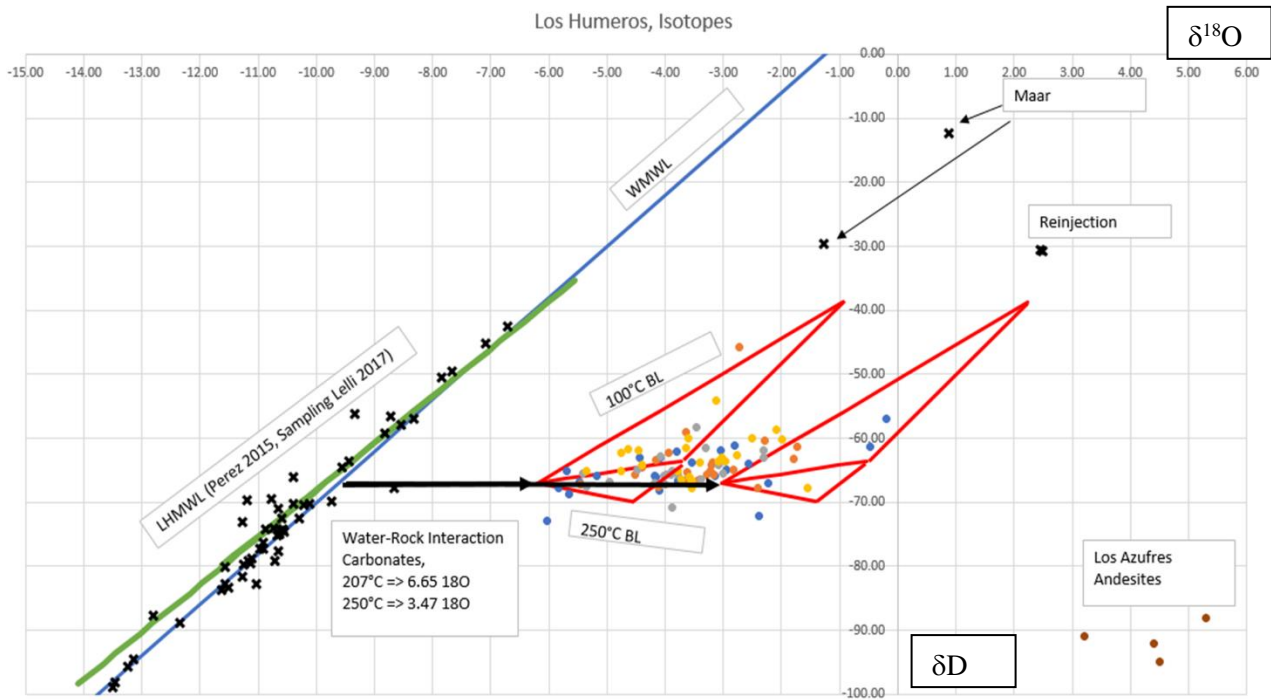


Figure 2.6: Stable Isotope distribution and boiling model

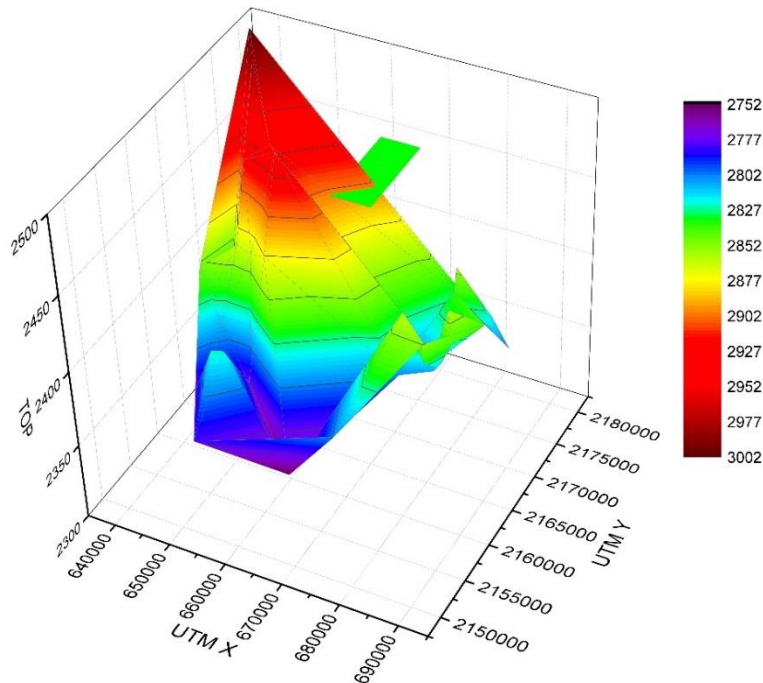


Figure 2.7: Hydraulic head (elevation of the water table in masl) in the area surrounding Los Humeros (the study area is evidenced as green rectangle, arbitrary elevation).

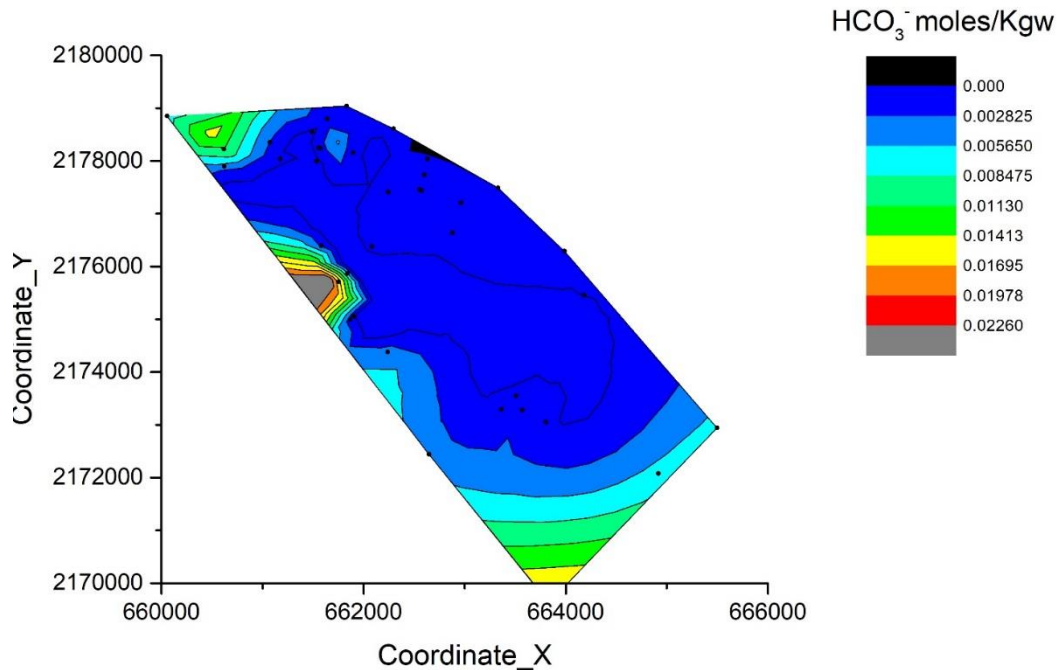


Figure 2.8: Bicarbonate in liquid phase, as representative of the recharge component evidenced in the geochemical investigation (Task 4.3)

In Figure 2.7, in spite of the few measures available (static water level of the surficial aquifer, data from CFE), we can observe that the water level of the surficial water table seems to point out that the recharge is likely to inlet the geothermal system from the west border. From the wells data, we know that the wells present as possible eastern expansion of the geothermal system, are hot but dry/not productive.

The western input of the recharge is evidenced also in the geochemical modeling (Task 4.3), in which the geothermal fluid origins is discussed with respect to the spatial distribution of its components, and a representative of the recharge components is reported in figure 2.8 (geothermal well fluid composition is a courtesy of CFE). In figure 2.8, we observe the bicarbonate in liquid phase spatial distribution, and it is linked to the regional circulation in limestone.

On these basis, it seems clear that the main recharge inlet from the western border of the geothermal prospect at the level of the shallow feed zone, with a temperature around 200- 250 °C, consistent with the average temperature of the shallow feed zone.

2.5 Hot source

In a “classical” geothermal system, in which the geothermal anomaly is not related solely to the regional geothermal gradient, one of the main important topic is in defining the hot source to define the best exploitation plan. It is correct to say that geothermal energy is related to efficiently “mine” the heat from underground. In Los Humeros a clear definition of the hot source by geophysical means is not available; however, we can have some constrain on its position and extent. In figure 2.9, we have the temperature map at the deep feed zone as obtained from the data in table 2.1. We should point out that the deep feed zone depth is different in the map. Here we have 3 temperature anomaly (hot zone) in the northern, central and southern part of the study area.

We can compare the temperature map with the geochemical modeling results, (from task 4.3) here represented by boron spatial distribution in figure 2.10. According to the investigation in task 4.3, Boron is defined as one of the markers of deep origin of fluids. In the boron spatial distribution map, we can recognize 3 high concentration area, similarly to the temperature map, in the northern, central and southern part.

The MT data published in Arzate et al., 2018 (figure 2.11), show generally 2 main intrusion at depth, but we cannot directly relate this data with the 3 anomaly clearly defined by both geochemical and temperature data. The most probable explanation that come to us, is that the northern and central anomaly are part of the northern hot intrusion with a slit due to local geology (fracture, open conduct) that led to the formation of the central anomaly, while the northern and southern anomaly are more directly related to the hot intrusion at depth evidenced by MT investigations.

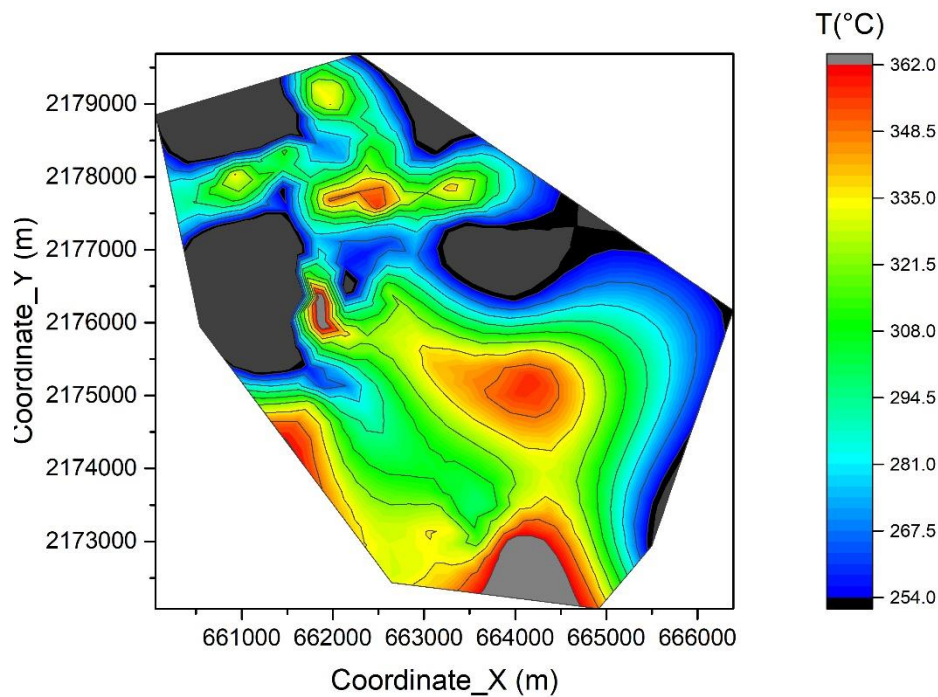


Figure 2.9: Temperature distribution at the deep feed zone

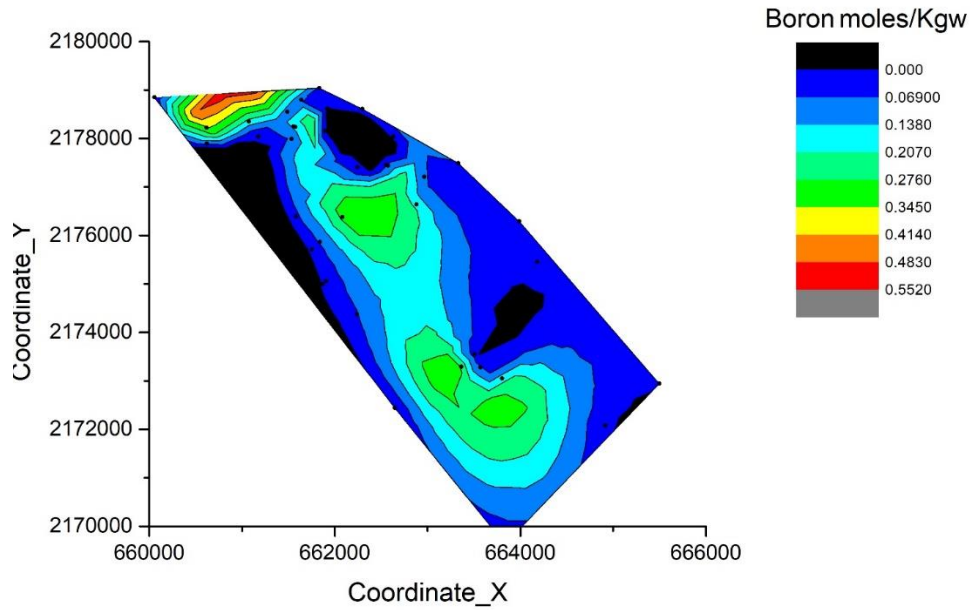


Figure 2.10: Boron distribution, from geochemical modeling Task 4.3

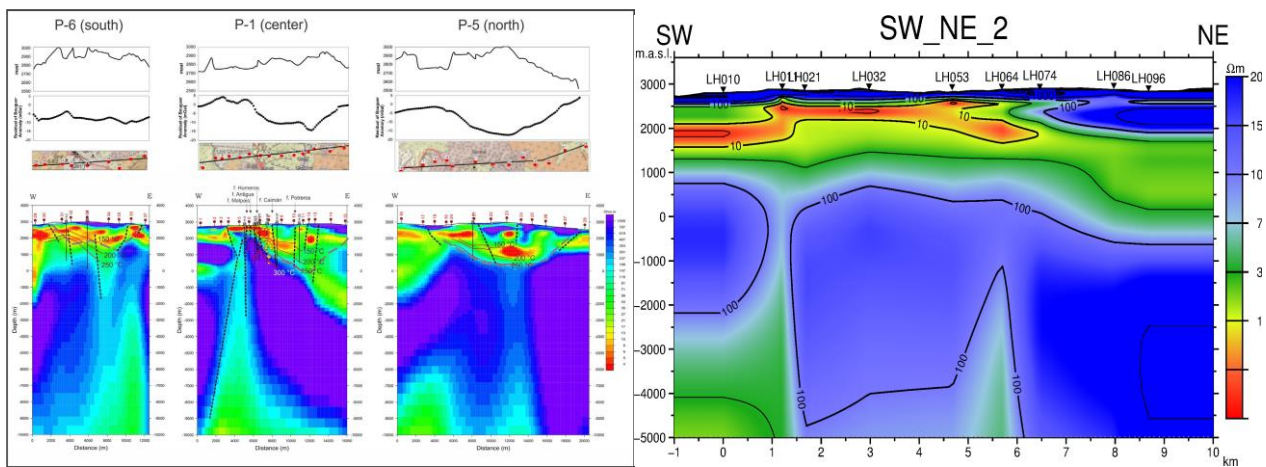


Figure 2.11: Resulting resistivity sections across the caldera edifice, Arzate et al., 2018, on left, and resistivity profile obtained during GEMEX project on right.

2.6 Feed zones and geological model

We reconstructed the top and bottom for a shallow and a deep feed zone using the data presented in table 2.1. To be able to do so, we had to regularize the surfaces by merging feed zones in case of more than two, but even more to correctly attribute, based on temperature and position, a given well feed zone to a common feed zone. After some work, only well H-50D was not defined in this approach; we can deduce that a very hot geothermal fluid reach well H-50D, that according to the neighboring wells is pertaining to the deep feed zones, but it is located at the level of the shallow feed zone. This behavior could be reproduced only accounting for a local fault providing the hot fluid.

By comparing the position and structure of the shallow and deep feed zone with the geological layers (Figure 2.12), a clear trend apart from the general deepening in the south direction, could not be found. Moreover, the relatively thin layer separating the two feed zone go across the Top Pre-Caldera unit. In this settings, it seems more probable to attribute this low permeability layer to a paleo and/or current hydrothermal alteration at depth. In a similar way, the top of shallow feed zone is separated from the surficial aquifer by self sealing (quartz, calcite and kaolinite) as commonly occur in geothermal system. The presence of skarn and hydrothermal alteration at temperature higher than 250 °C is also a common occurrence in geothermal systems.

A detail of the relation of the Deep Feed zone with Top Basement and Top Pre-Caldera unit is shown in Figure 2.13. The feed zone goes below the Top Basement layer, and in many places over the Top Pre-Caldera unit that consequently are not a constrain for the deep feed zone.

The same is true for the shallow feed zone (Figure 2.14), that come across the Top Basal Pre-Caldera and is below, with a complete different geometry, to the Inter Pre Caldera unit top.

As results, we cannot attribute a defined lithotypes to the shallow and depth feed zones or impermeable layers, but only generically conclude that are usually locate in the andesite.

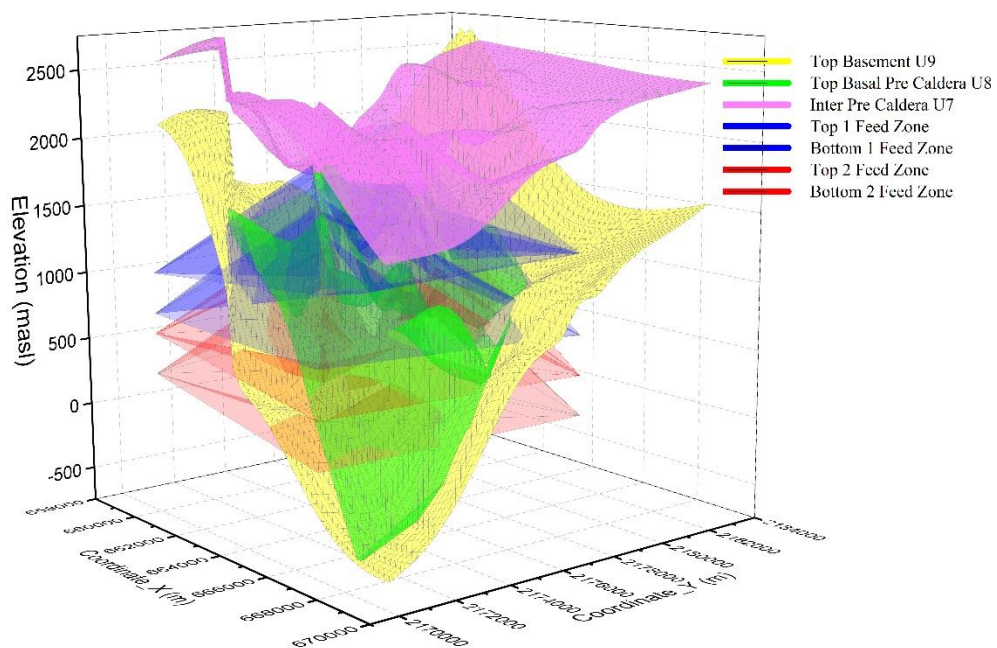


Figure 2.12: Feed zones position with the neighbouring geological layers from the local geological model of Los Humeros

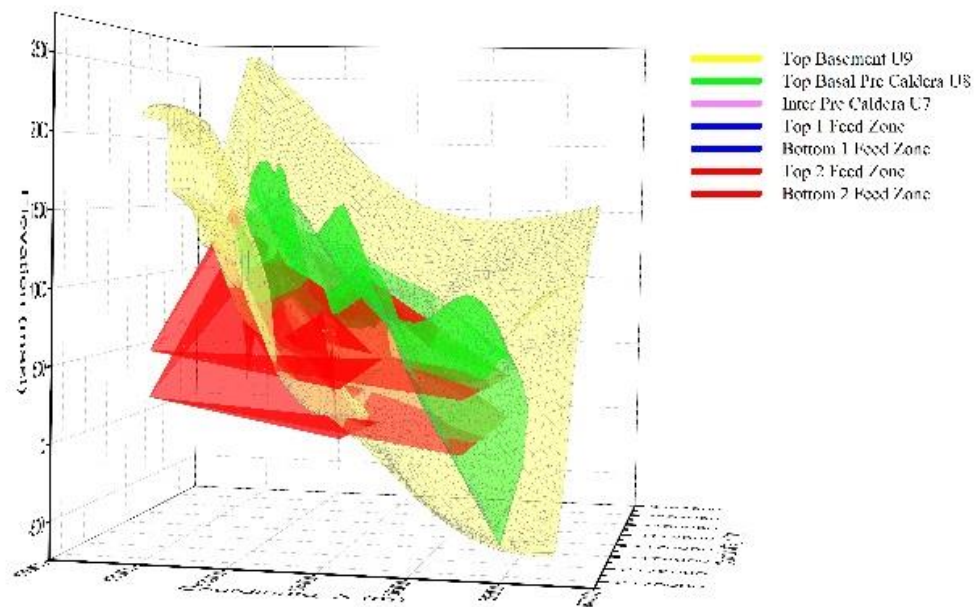
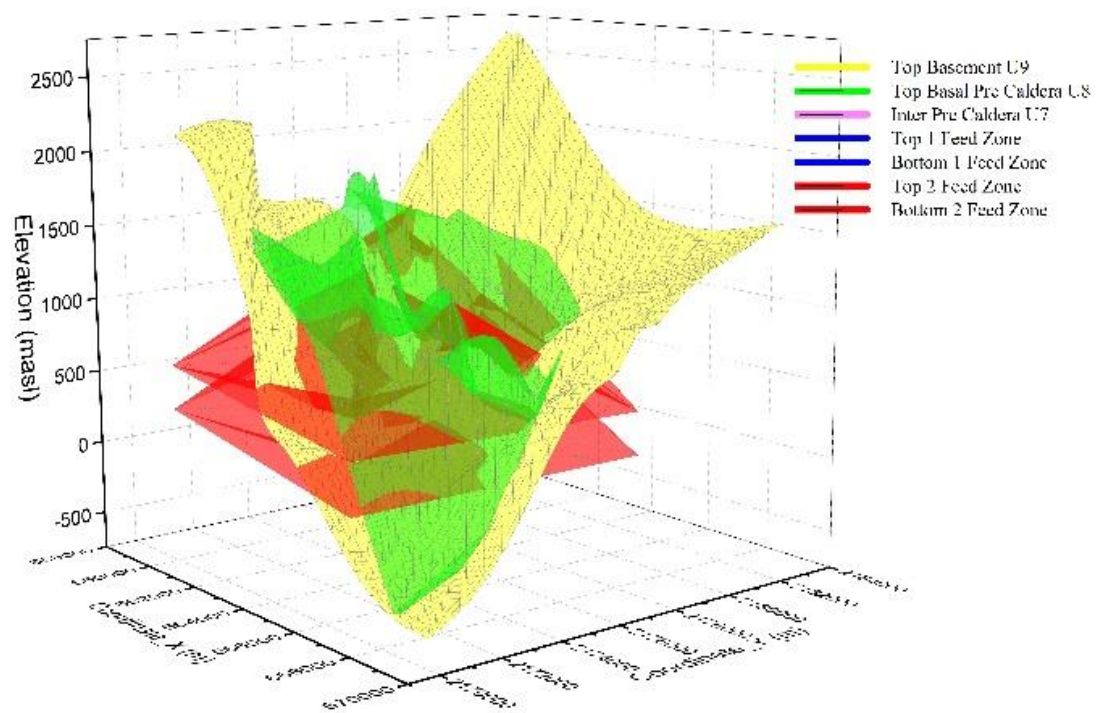


Figure 2.13: Detail of the deep Feed zone with Top Basement and Top Pre-Caldera unit, top - view from south west, bottom - view from west.

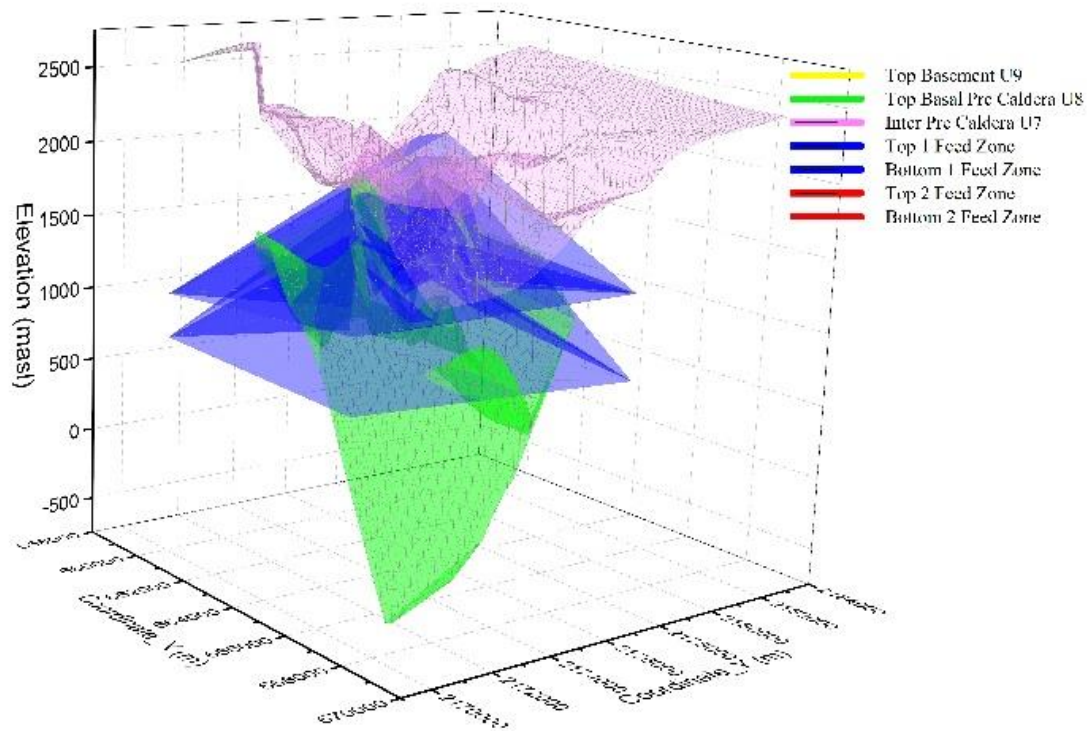


Figure 2.14: Detail of the shallow Feed zone with Top Basal Pre-Caldera unit and Inter Pre-Caldera unit -view from south west.

2.7 Permeability and porosity

An evaluation of the permeability for Los Humeros geothermal field could be obtained mainly from three different approaches:

- 1) Production model
- 2) Pumping step tests
- 3) Sample measurements

Here we will describe shortly the different methods and their results.

The production model use a 2D radial model, computed by means of Hawkin's formula (Hawkin's 1956), the reservoir pressure and well bottom pressure (obtained from wellbore fluid flow model, Appendix A). In the Hawkin model, the production is related to a 2D radial reservoir model with skin factor (S that usually is set to 0 or -1 for geothermal system, if unknown). In the equation B is the production flow, μ water viscosity (accounting the different phases), r_e/r_w the relative exploitation distance, p_e the reservoir pressure, p_w the well bottom pressure and k the permeability. The wellbore model is here needed to have the correct well bottom pressure and phase ratio (dryness or steam/fluid ratio).

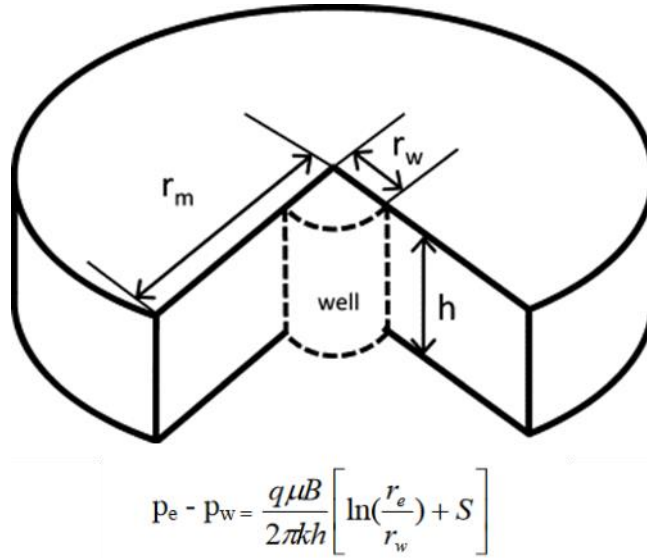


Figure 2.15: Hawkin's radial model schematic

The permeability per meter obtained in the Hawkin's Kh model resulting from the production model have median value of 2.22×10^{-12} Darcy*m (median value, ranging from 5×10^{-13} to 5×10^{-11}), that using the feed zone thickness corrected for well completion could be converted in 4.4×10^{-15} m². In this conversion, the difficulties arise in evaluating the effective feed zone thickness to compute the permeability after the result of the Kh model; we have to take in to account the effective well completion, and in the feed zones could be present a non-flowing zone (e.g. evidenced in the temperature dynamic log of well H-59 in figure 2.1 and A.1) that we may not be aware of.

The pumping step tests (Horne 1995, Earlougher 1977) is modeled following a Theis model. The results in terms of Darcy per meter from the Kh Theis model are similar to the permeability from production model above described, but slightly lower, with a median value of 1.67×10^{-12} Darcy*m. An example is well H-43, here reported in figure 2.16, that have 720 mD*m and if we consider a thickness of the productive layer of about 300 m (1st feed zone only) we obtain a permeability of 2.9 mD. Following the same reasoning, with many difficulties in defining the effective feed zone thickness for injection (that may be different with respect to feed zone for production), we obtain a median permeability of about 3×10^{-15} m² with values ranging $1.25 \times 10^{-15} - 5 \times 10^{-15}$.

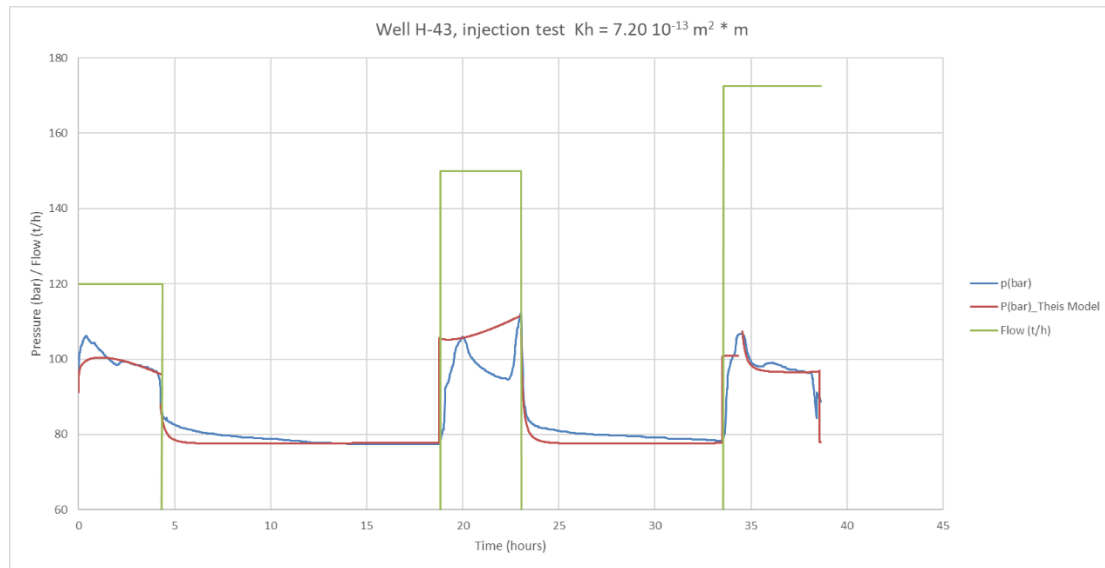


Figure 2.16: This model of pumping step test from well H-43

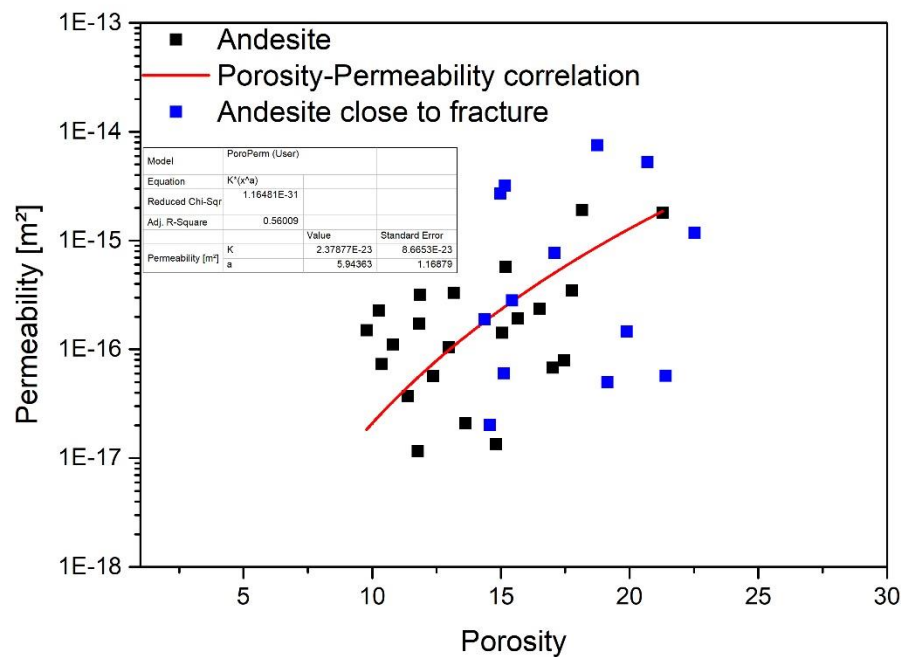


Figure 2.17: Porosity and permeability investigation on andesite from Los Humeros geothermal field

The samples porosity and permeability measurements are results of Task 6.1; from the results, we extracted the values for andesites only, that on turn are divided in andesite and andesite close to fracture. According to Farquharson et al., 2015, Lamur et al., 2017, andesites from volcanic edifice have a weak porosity – permeability correlation. In figure 2.17 we report the same investigation for the measurements carried out on andesite in task 6.1, and using the proposed equation

$$K = K_0 * \phi^\alpha$$

Where K is permeability, ϕ is porosity and α and K_0 are constant to be fitted.

We are able to identify a weak ($R^2 = 0.56$) correlation in our samples as well. In the measurements, the obtained permeability is higher with respect to the values obtained with the other 2 approach. Here we have to take in to account that the lab confining pressure used for permeability measurements is lower than the confining pressure in the reservoir, thus this values should be corrected by using their compressibility (not available). Heap et al., 2016, report the permeability-confining pressure correlation for an andesite from Colima Volcano. A similar correlation is expected for Los Humeros andesites, too, since this could explain the difference between the results of the production model, pumping step tests and sample measurements.

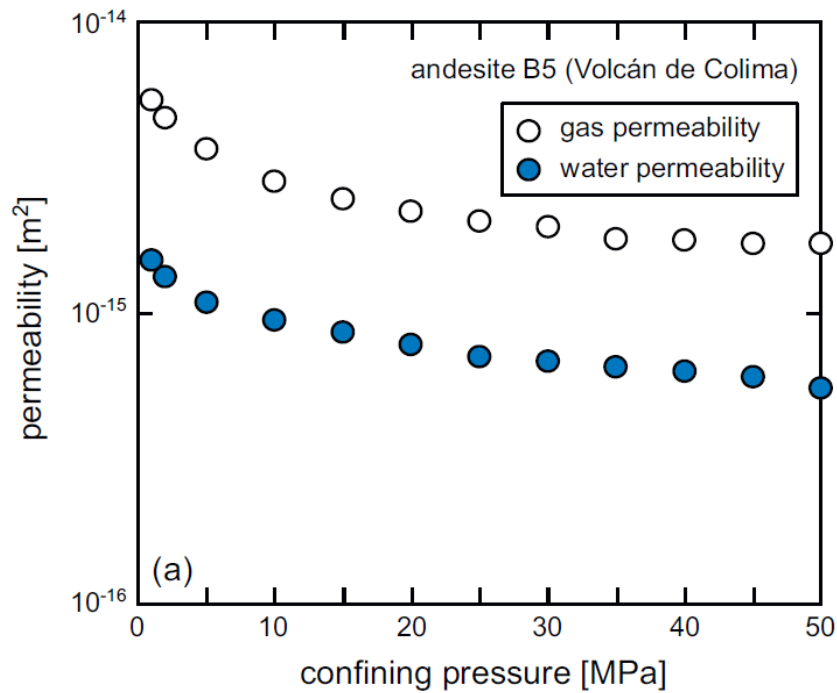


Figure 2.18: Permeability of Colima volcano with respect to confining pressure

On the basis of what discussed so far, we can attribute a value of $3.0 \times 10^{-15} \text{ m}^2$ to the feed zones, and 1.0×10^{-16} - 10^{-17} m^2 to the not permeable layers in between and below. Due to the self-sealing that commonly occur in geothermal systems at the condensation level, and to have an effective separation with the surficial aquifer, we assume that the seal between surficial aquifer and first feed zone have a permeability of 1.0×10^{-26} .

2.8 Thermal capacity and conductivity

In order to obtain a representative values for thermal capacity, we used as reference the average values measured in Task 6.1 for andesites (0.768 J/Kg) and computed its temperature dependence according to Schön, 2011 in which the thermal capacity is given by the weighted average of the thermal capacity of its minerals. To have a representative andesite composition, we used the sample Rugg 4 (Task 4.3, sample of a Los Humeros andesite), and then corrected the value at lab temperature to match the average saturated value measured. The resulting value of heat capacity vs temperature are in figure 2.19.

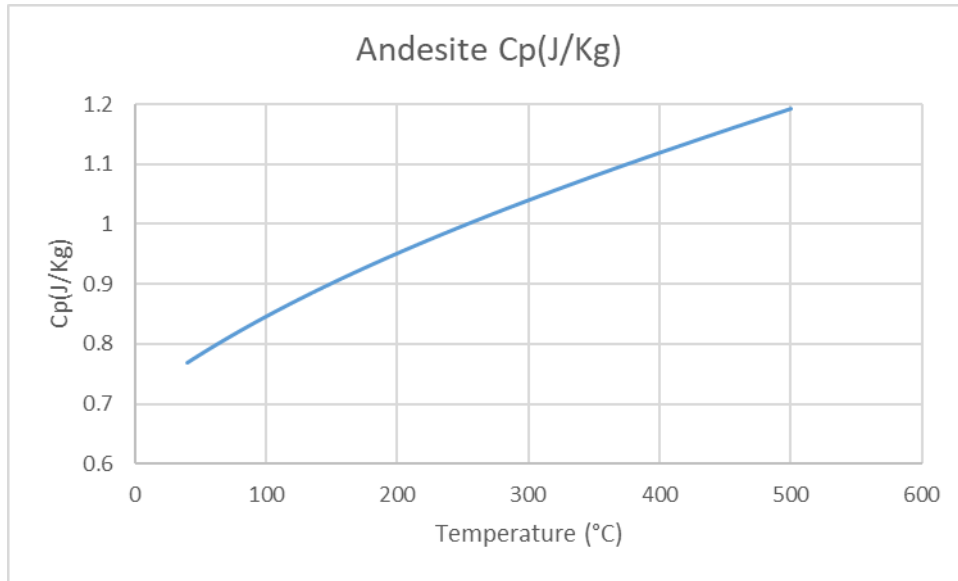


Figure 2.19: Los Humeros Andesite heat capacity vs temperature

A similar approach was used for the thermal conductivity. We used the average heat conductivity (saturated) value at lab temperature as starting point, and then we used the correlation proposed by Vosteen et al.,(2003), for volcanic rocks to compute its temperature dependence; the results with minimum and maximum values are in figure 2.20.

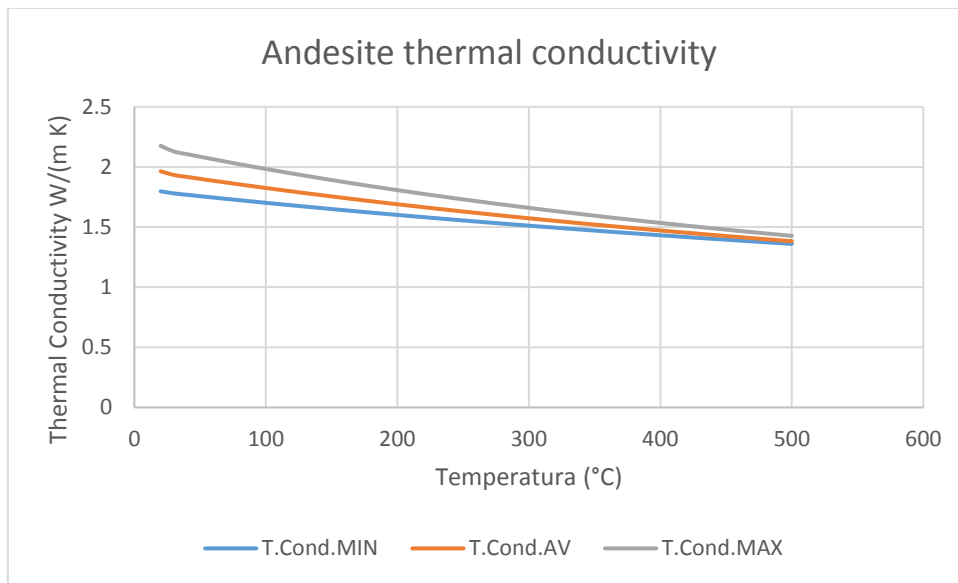


Figure 2.20: Los Humeros andesite thermal conductivity vs temperature

2.9 Numerical model

The geothermal industry has a thriving research sector, which has developed several software codes for modelling purposes. Some of these codes have become widely used within the industry and are commercially available. Typically, these codes have a long history, though their designs rooted in the 1980s. Very few of these codes focus on the flexibility and robustness required by the geothermal industry, nor they

attempt to integrate models from different disciplines. Limitations in the existing numerical, geophysical and chemical modelling tools have challenged the geothermal industry and research community for the last decades. Efforts are spent attempting to overcome these limitations in order to address current day issues.

TOUGH2 (Pruess, 2003) has been a success story for the geothermal modelling community and has been widely adopted for geothermal reservoir modelling and many other applications. This success is due to a combination of factors including availability at a relatively low cost with full access to source code and design decisions that allowed limited extensions to the code.

In this study, the simulation of the natural state a 3D model was built using the TOUGH2 V.2.1 (Pruess et al. 2012) numerical reservoir simulator extended for water supercritical conditions by using IAPWS-IF97 formulation (DESCRAMBLE, D5.3, H2020, Grant Agreement No - 640573) managed by using the Petrasim pre- and post-processing software package. These extensions were needed to overcome the temperature limit (350 °C) of the previous TOUGH2 version, to be able to model super-hot and supercritical geothermal systems, such as that of Larderello at depth.

In Figure 2.21, the modelled area for TOUGH 2 local model is evidenced within the geological map of Los Humeros caldera and geothermal field.

On the basis of the position of geological layers and feed zones, the formation of interest consist of, (according to Carrasco et al., 2017):

Pre-volcanic basement. The pre-volcanic basement is composed of Mesozoic limestone and shale metamorphosed to different grades. In the majority of the cases, the alteration formed hornfels and skarn, which are accompanied by the intrusion of andesite-like and diabase rocks with occasional granodiorite.

Pre-caldera group. This group includes a thick succession of more than 1500 m on average. It is dominated by pyroxene andesitic lavas, and minor horizons of basaltic and rhyolitic-dacitic lavas.

Basal pre-caldera unit.- miocene hornblende-bearing andesites and basalts. This unit is restricted to the bottom of a few wells, and it has no lateral continuity with the other wells.

Intermediate pre-caldera unit- pyroxene-bearing porphyritic andesites. This unit includes the thickest part of the andesitic pre-caldera succession. It comprises dominantly pyroxene-bearing microporphyritic andesite lavas, with rare mafic andesites at the basal part or with a dacitic affinity.

Since there is not a clear correlation among feed zones and geological units, the attribution of a rock type results very difficult. However, given that in the formation encompassing the two feed zones andesite is recognized as one of the main rock type, we can refer to andesite for the petrophysical properties of the geothermal system. Regarding the petrophysical properties, we will refer here to the ones measured in task 6.1 for andesite and discussed in section 2.7 and 2.8.

bottom of the model was set to -2000 m.a.s.l. The study area shown in figure 2.21 represent the local model extension with the available wells with the geological map of the area. The model is defined by the following layers:

- 1) Top boundary, layer defined by Digital Elevation Model
- 2) Water table elevation (interpolated from water static levels, CFE data)
- 3) Top of the first feed zone
- 4) Bottom of the first feed zone
- 5) Top of the second feed zone
- 6) Bottom of the second feed zone
- 7) Bottom of the model at -2000 m

The numerical model is discretized with 30x40x21 elements, for a total of 28800 cells.

2.9.2 Boundary conditions

The recharge is defined in task 6.2, and here implemented in the model as a series of constant P,T elements along the west border of the geothermal prospect, as reported in figure 2.22. In red are evidenced the recharge boundary elements, while in blue are the other grid cells at bottom of first feed zone with the geological map intersection at 1100 m asl. The pressure of the recharge boundary elements is obtained from the pivot point pressure gradient.

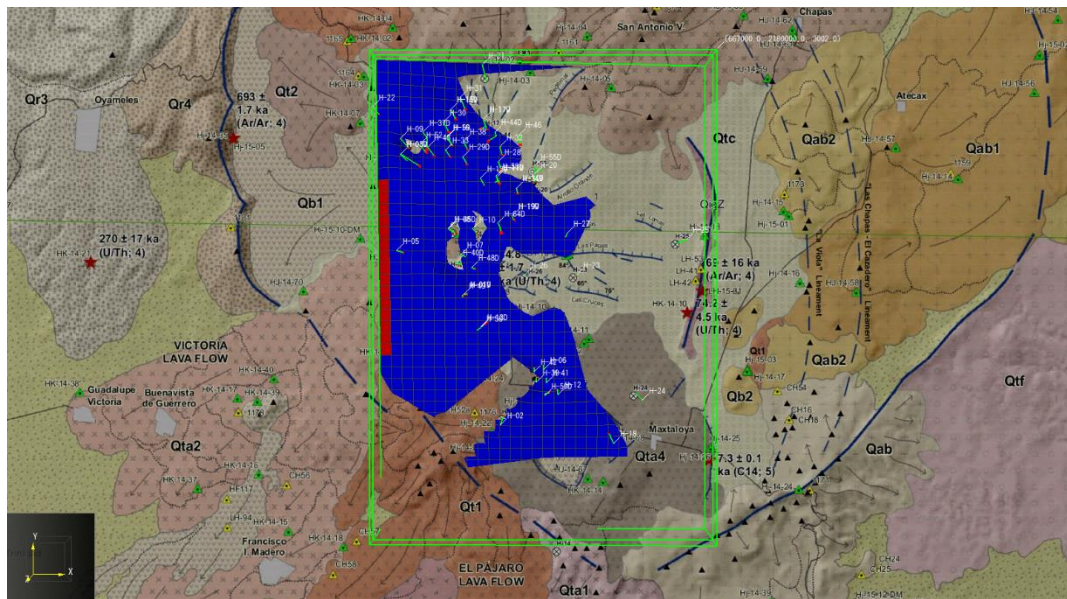


Figure 2.22: Recharge boundary

The top boundary condition is situated at the water table level, in order to have 1 bar of pressure with liquid water, that have a temperature ranging 40-90°C in the modeled area.

The bottom boundary condition consist of element at fixed temperature of 400°C, that start from -2000 m a.s.l. and during the steady state (3D natural state model) is shifted upward until a match of the steady state temperature and the temperature measured at the feed zones is obtained. This work were needed because we have only hint on the position and temperature of the hot intrusion, but not a clear definition of it. Hence, by moving the position of the bottom boundary at a fixed temperature of 400°C, we were able to reproduce the measured temperatures and we have as result a calibrated steady state model and a better definition of the hot intrusion.

2.9.3 Steady state

After a long runtime, the numerical model stabilize on a set of P,T,X conditions (Steady State) that are assumed as representative of the natural state of the system.

In figure 2.23 (left) the temperature distribution at 0 m asl could be observed, with the 2-phase zone (figure 2.23 right, violet cloud). The 2-phase zone around the northern sector of the geothermal field were previously found in figure 5, PT diagram, and here reproduced.

In figure 2.24 the temperature distribution at 500 m asl could be observed, with the 3 thermal anomaly that correspond namely to the north, central and south sector of the geothermal system. The north and central section of the geothermal system do not have a net separation, as could be seen in figures 2.24, 2.25 and 2.26. Figure 2.25 show temperature distribution (view from east) with the main upflow corresponding to the northern sector and the downflow corresponding to the recharge.

In figure 2.26, temperature distribution at -250 m. The shape of the bottom boundary condition (400°C) could be observed (figure 2.25 and 2.26, orange contour).

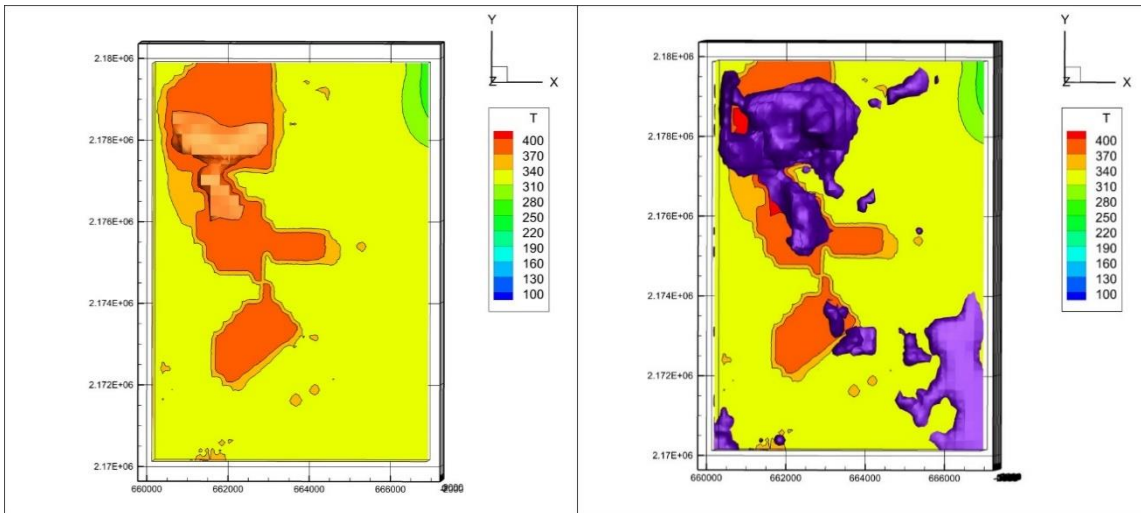


Figure 2.23: Temperature distribution at 0 masl (left figure) and with the 2-phase zone (figure on right, violet cloud is the 2-phase zone)

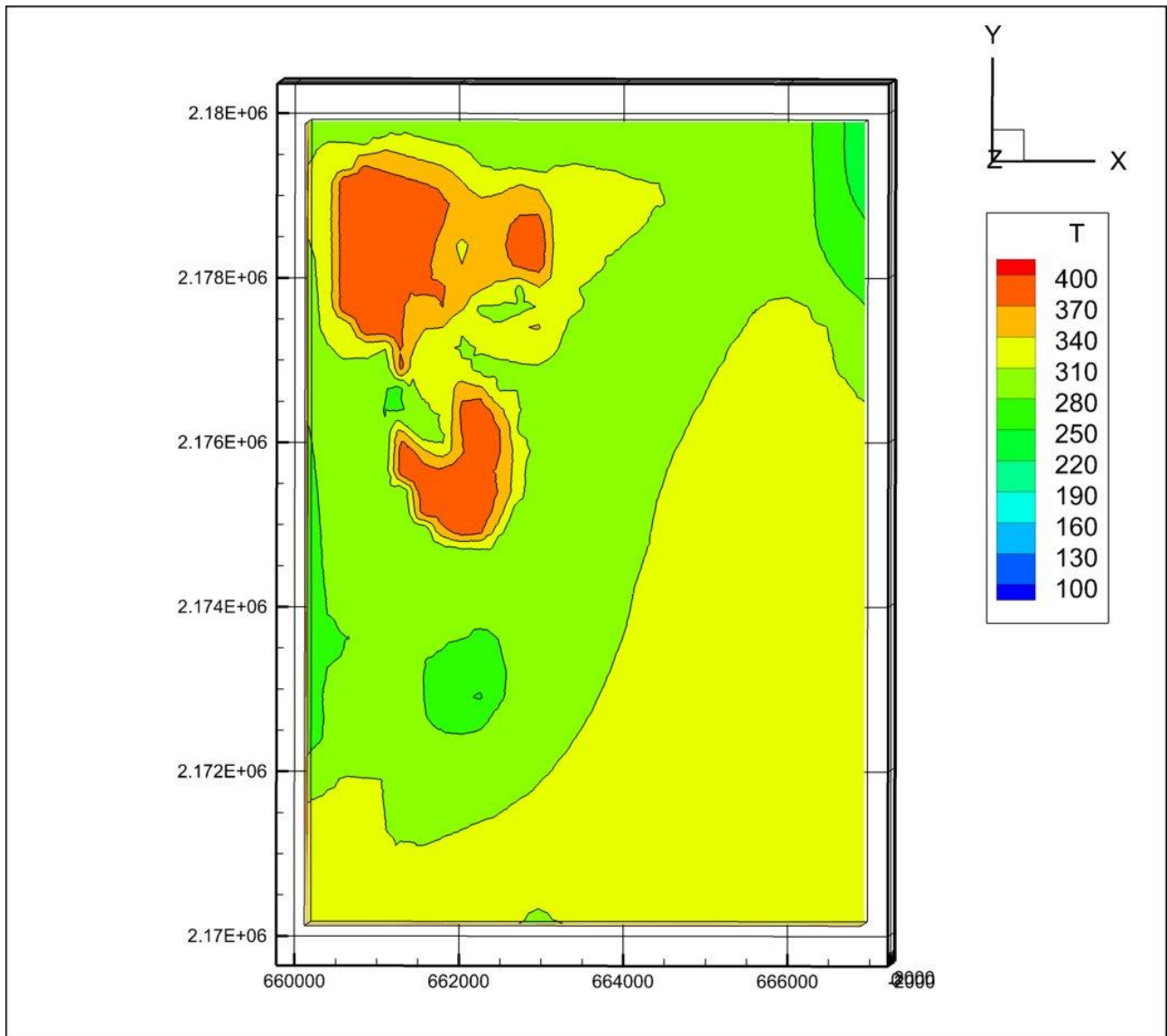


Figure 2.24: Temperature distribution at 500 m asl. The 3 temperature anomaly could be identified.

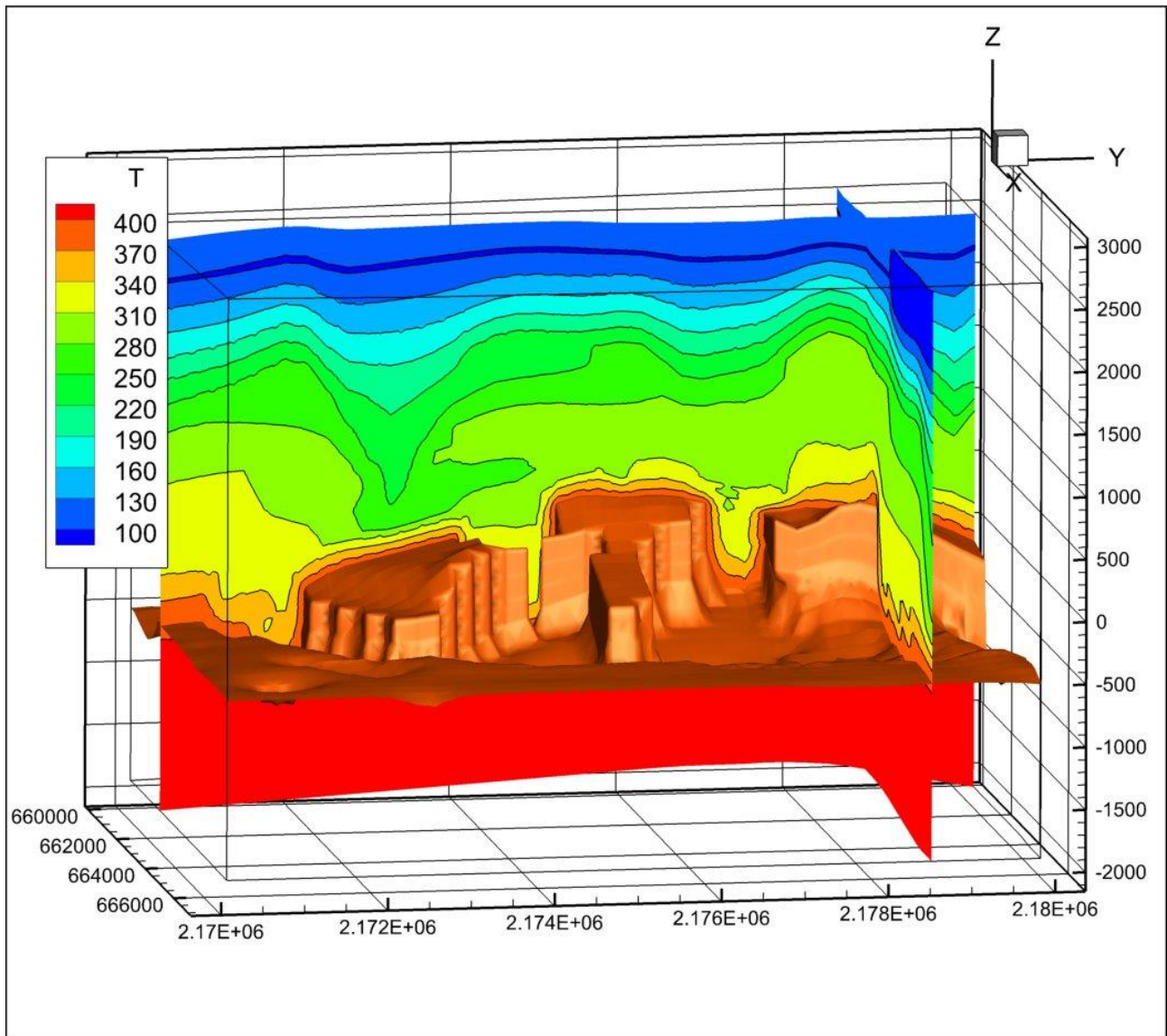


Figure 2.25: Temperature distribution, view from east, with the 400°C bottom boundary condition (dark orange surface).

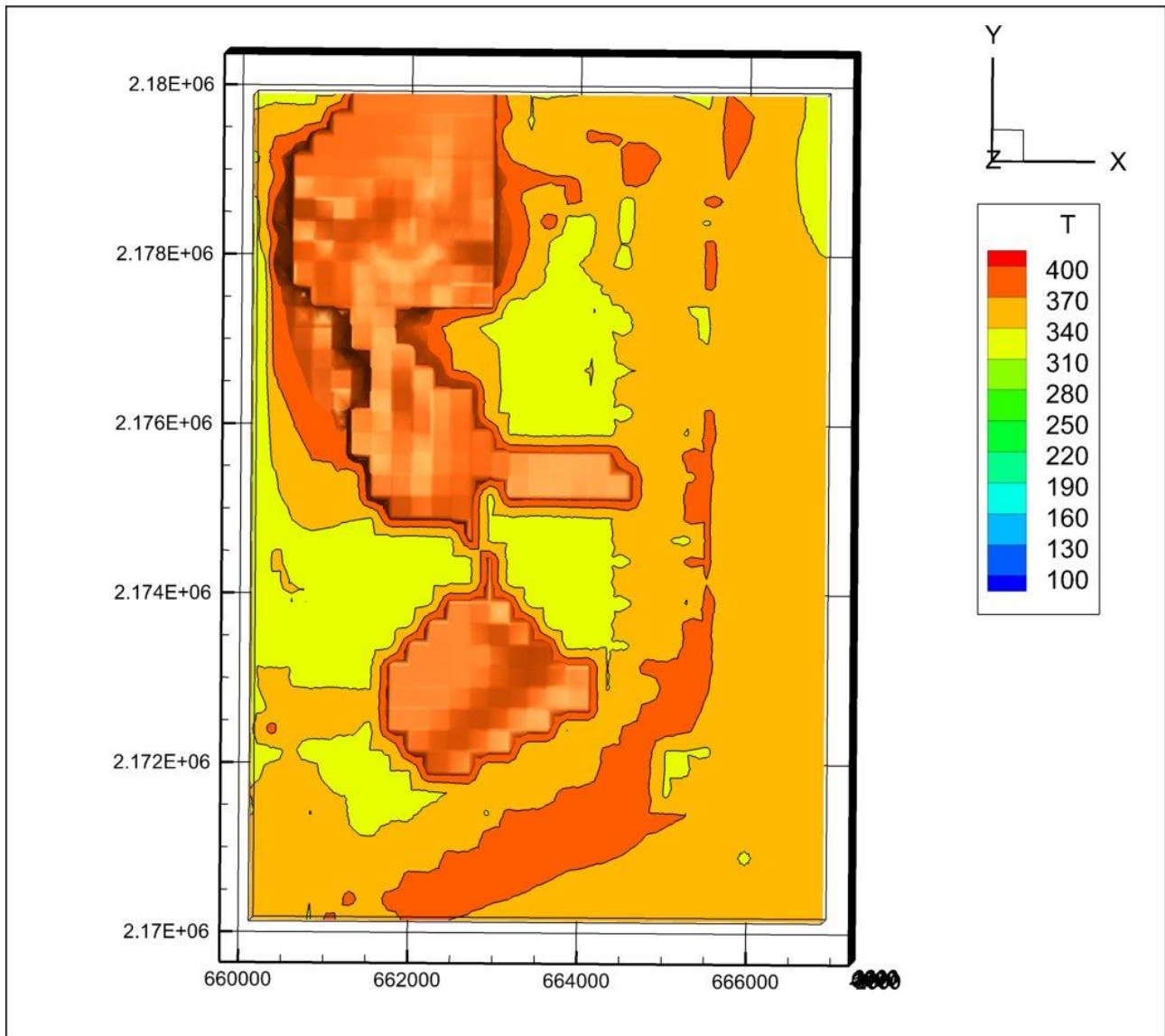


Figure 2.26: Temperature distribution, with a slice at -250 m asl, and the 400°C bottom boundary condition (dark orange surface).

2.9.4 Calibration

From the resulting temperature distribution, we can compare the temperature of the two feed zones as modeled with the temperature obtained from well logs in table 2.1.

In this paragraph, we refer to the stabilized temperature extrapolated from temperature logs during heating up, as measured temperature, even if this is not strictly true.

The process of identifying a feed zone and then compute its temperature by using Horner method, cylindrical or spherical heat source or other method have an intrinsic error that is even greater than what we obtain from the direct computing (different person may provide different results). In this context, missing a “true value” for estimating the measurement error, we will attribute a generic 10% error to the measured data (extrapolated temperature).

In figure 27 the correlation between feed zone temperatures (named measured temperatures) and the corresponding temperatures from the model is shown. We can observe a good correlation, and generally the distribution is close to the 1:1 line.

The overall Nash-Sutcliffe coefficient is 0.82, but its value is affected mainly by the lower temperature values related to the shallow feed zone. These values may have contribution from the shallower aquifer, infiltration due to fracture or induced while drilling, and generally very difficult to introduce in a model because very localized (e.g. close by or in between to higher temperature points).

The Nash-Sutcliffe coefficient of 0.82 correspond roughly to an 80% accuracy of the model, and it is consistent with the 10% error attributed to the temperature data. The resulting P, T, composition distribution calibrated so far and the corresponding model are available for further investigation on request.

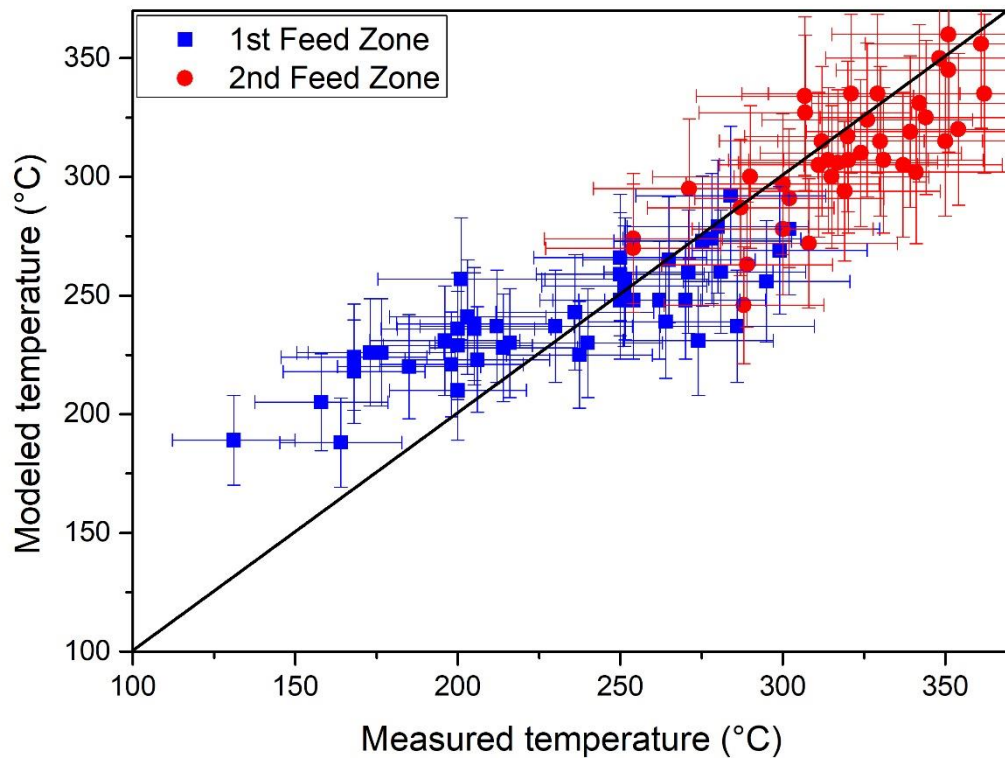


Figure 2.27: Model calibration: modeled temperature vs temperature from well logs (measured temperature)

2.10 References

- Arzate J., Corbo-Camargo F., □, Carrasco G., Hernández J., Yutsis V., “The Los Humeros (Mexico) geothermal field model deduced from new geophysical and geological data”, *Geothermics* 71 (2018) 200–211
- Carrasco-Núñez G., López-Martínez M., Hernández J., Vargas V., “Subsurface stratigraphy and its correlation with the surficial geology at Los Humeros geothermal field, eastern Trans-Mexican Volcanic Belt”, *Geothermics* 67 (2017) 1–17
- Earlougher R.C.: *Advances in Well Test Analysis*, 1977, 264 pp., SPE Monograph Series, Vol. 5, ISBN: 978-0-89520-204-8
- Farquharson J., Heap M.J., Varley N.R., Baud P., Reuschlé T., “Permeability and porosity relationships of edifice-forming andesites: A combined field and laboratory study”, *Journal of Volcanology and Geothermal Research* 297 (2015) 52–68
- Grant M., Bixley P., *Geothermal Reservoir Engineering*, 2nd Edition, ISBN: 9780123838810, Academic Press, 2011, pp 378
- Hawkins, M.F.J. 1956. A Note on the Skin Effect. *J Pet Technol* 8 (12): 65–66. SPE-732-G.
<http://dx.doi.org/10.2118/732-G>
- Heap M.J., Reuschlé T, Farquharson J.I., Baud P., Permeability of volcanic rocks to gas and water, *Earth and Planetary Science Letters* 447 (2016) 139–150
- Horne, R. N., 1995. *Modern Well Test Analysis: A Computer-Aided Approach*, 2nd. ed., Petroway, Palo Alto, 257p
- Lamur A., Kendrick J. E., Eggertsson G. H., Wall R. J., Ashworth J. D. , Lavallée Y., “The permeability of fractured rocks in pressurised volcanic and geothermal systems”, *Scientific Reports*, 2017, 7: 6173 , DOI:10.1038/s41598-017-05460-4
- Pruess K. (2003). *The TOUGH Codes - A Family of Simulation Tools for Multiphase Flow and Transport Processes in Permeable Media*. Earth Sciences Division, Lawrence Berkeley National Laboratory University of California, Berkeley, CA 94720
- Pruess, K., Oldenburg, C., Moridis, G. (2012). *TOUGH2 USER’S GUIDE, VERSION 2*, Earth Sciences Division, Lawrence Berkeley National Laboratory, University of California, Berkeley, California 94720, LBNL-43134
- Schön, J. H. (2011). *Physical properties of rocks: Fundamentals and Principles of Petrophysics*, volume 8. Elsevier Science & Technology, Amsterdam.
- Vosteen H.D., Schellschmidt R., Influence of temperature on thermal conductivity, thermal capacity and thermal diffusivity for different types of rock, *Physics and Chemistry of the Earth* 28 (2003) 499–509

Appendix A - Wellbore fluid flow modeling

The HOLA multi-component, multi-feedzone geothermal wellbore simulator is used to carry out the flowing well modeling. This simulator reproduces the measured flowing temperature and pressure profiles in flowing wells and determines the relative contribution, fluid properties (e.g. enthalpy, temperature) and fluid composition (e.g. CO₂, NaCl) of each feedzone for a given discharge condition.

In our case many wells have data on discharge condition measured at well-head, and we used the P,T conditions at depth found so far for the feed zones to model the flowing condition.

This modeling helps in clarifying the contribution of the feed zones to the well production, and provides the P, T, Enthalpy and steam/brine ratio along all the well profile, down to the well bottom.

Starting from the wellhead data during production, and well geometry, we can have a flowing well model that computes the P,T, Enthalpy profile of the well.

The HOLA multi-component, multi-feedzone geothermal wellbore simulator is used to carry out the flowing well modeling.

This simulator reproduces the measured flowing temperature and pressure profiles in flowing wells and determines the relative contribution, fluid properties (e.g. enthalpy, temperature) and fluid composition (e.g. CO₂, NaCl) of each feedzone for a given discharge condition.

In our case many wells have data on discharge condition measured at well-head, and we used the P,T conditions at depth found so far for the feed zones to model the flowing condition. An example of modeled wellbore flowing profile is in figure 28 for well H-59; in this case, by looking at the dynamic temperature log, we can observe a non-flowing zone at well bottom.

This modeling helps in clarifying the contribution of the feed zones to the well production, and provides the P, T, Enthalpy and steam/brine ratio along all the well profile, down to the well bottom. This is useful in the framework e.g. of geochemical modeling, to clearly define the phase segregation problem i.e. the amount of steam phase (figure 29) and the phase partitioning along the well profile.

Unfortunately in some cases the direct comparison between measured and modeled flowing condition could not be done because the wellhead condition (P,T, Flow Rate and steam/total flow ratio) used for the wellbore modeling were obtained from the production data and are different from the one present during flowing well P,T measurement.

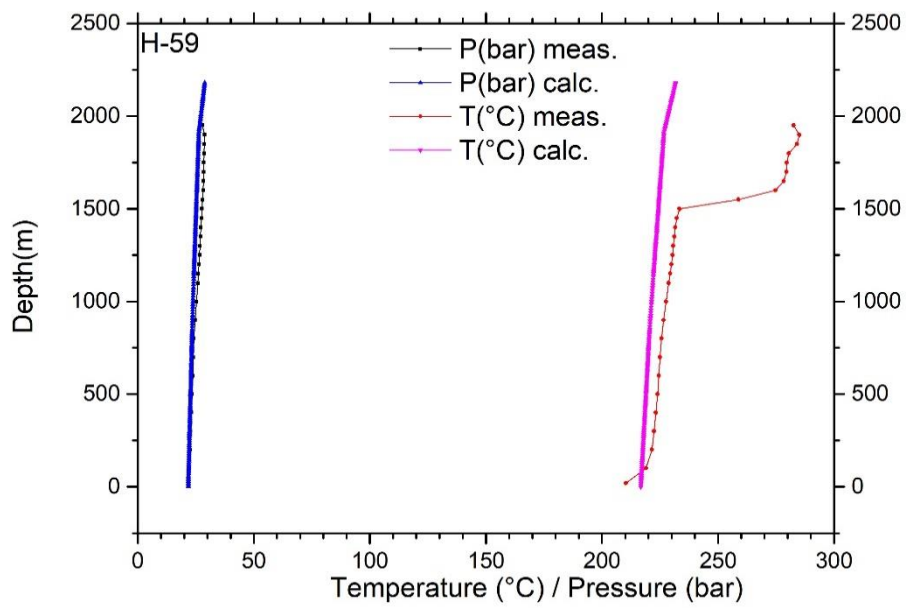


Figure 2.28: Temperature and pressure profile from wellbore model compared with temperature and pressure from dynamic log

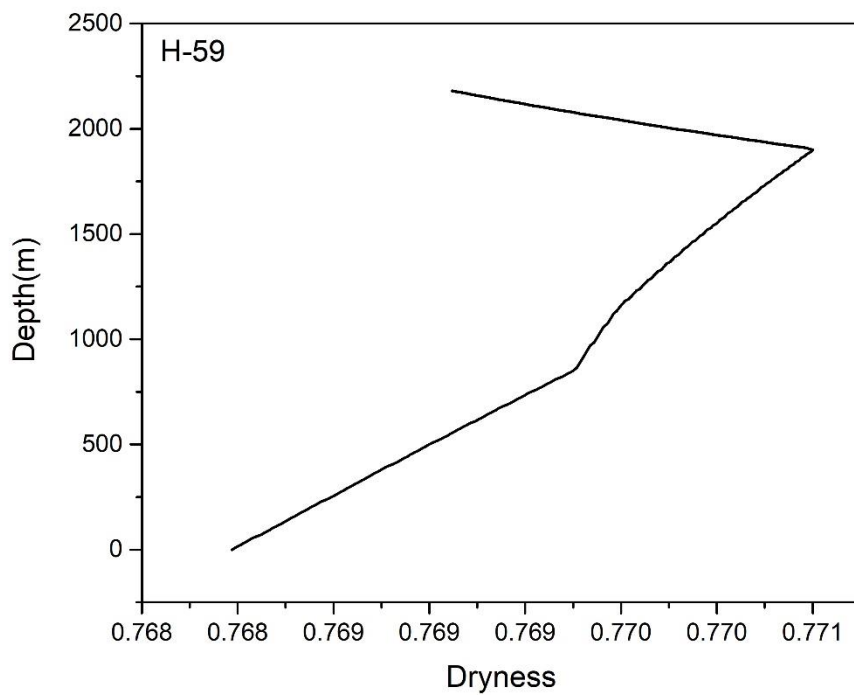


Figure 2.29: Dryness profile, where dryness is steam flow divided by total flow



Coordination Office, GEMex project

Helmholtz–Zentrum Potsdam

Deutsches GeoForschungsZentrum

Telegrafenberg, 14473 Potsdam

Germany